Optimal design and comparison of 2-X and 2-R planar cable-driven tensegrity-inspired manipulators

Vimalesh Muralidharan, Philippe Wenger, Christine Chevallereau

Optimal design and comparison of 2-X and 2-R planar cable-driven tensegrity-inspired manipulators

Vimalesh Muralidharan [*,†] Philippe Wenger[‡] Christine Chevallereau[‡]

Abstract

In this paper, we perform the design optimization and comparison of two tensegrity-inspired manipulators, composed of two anti-parallelogram (X) joints and two revolute (R) joints, respectively. These manipulators are equipped with springs and are actuated remotely with four cables each. In our recent article [1], the conditions for the mechanical feasibility of springs and bars have been discussed for the two manipulators, followed by the computation of their stable wrench-feasible workspace (SWFW). Building on that work, in the proposed paper, we design the 2-X and 2-R manipulators to carry a given point mass payload over a disk of a specified radius while minimizing their maximal actuation force, moving mass, and size. We present the Pareto optimal fronts for the two manipulators and compare several designs from them. Then, we study the variation of the chosen objectives for different payload and disk radius specifications for the two manipulators to determine which one is better under what circumstances. Finally, we illustrate that the proposed optimization scheme can also be applied to other design scenarios with minimal changes.

Keywords: Tensegrity-inspired manipulators, Stable wrench-feasible workspace, Optimal design, Pareto front

Nomenclature

DoF	Degree(s)-of-freedom
X	Anti-parallelogram joint
R	Revolute joint
l, b	Lengths of bars in the X-joint
r, h	Semi-base length, height of isosceles triangles in the R-joint
α_i	Orientation of the top bar of the i^{th} joint w.r.t. its base
$\overline{\overline{\alpha_{\max}}}$	Upper bound for α_i due to geometry of the joint and cable actuation
σ_α	Fraction $\in]0, 1[$ used to set safe joint limits
$\overline{\alpha_{\max}}$	$(< \overline{\overline{\alpha_{\max}}})$ safe upper bound for α_i inside the limits due to geometry and actuation
$k_i, l_{0_i}, l_{\max_i}$	Stiffness, free length, maximum operating length of springs installed in the i^{th} joint
$\alpha_{\max_i}$	$(\leq \overline{\alpha_{\max}})$ actual upper bound for α_i considering the spring free length (l_{0_i})
d, D, N_a	Wire diameter, nominal coil diameter, number of active coils of a spring
r_{b_j}, m_j	Cross-section radius, mass of the j^{th} bar in a manipulator
$F_{\max}$	Maximum bound on the cable forces
m_{p}	Mass of the point mass payload at the end-effector
SWFJ	Stable wrench-feasible joint space (α_1, α_2) of a manipulator
SWFW	Stable wrench-feasible workspace (x, y) of a manipulator
WFW	Wrench-feasible workspace (x, y) of a manipulator

1 Introduction

Robot manipulators can be broadly classified into two types: serial and parallel. The serial manipulators contain links and motors arranged serially in a successive manner. They have a large workspace, but incur the cost of heavy moving masses and massive energy consumption due to the floating actuators. In contrast, the parallel manipulators contain a moving platform and a fixed base connected through several serial chains, each of which typically includes one actuator fixed to the ground. They have a smaller workspace but benefit from small moving mass and low energy requirements. This work considers a new class

*Corresponding author

†Département of Mechanical Engineering, Université Laval, Québec, QC G1V 0A6, Canada.

‡Nantes Université, Ecole Centrale de Nantes, CNRS, LS2N, 44321 Nantes, France.

E-mail addresses: m.vimalesh94@gmail.com (Vimalesh Muralidharan), Philippe.Wenger@ls2n.fr (Philippe Wenger), Christine.Chevallereau@ls2n.fr (Christine Chevallereau).

of manipulators shown in Fig. 1, referred to as tensegrity-inspired manipulators [1]. They have a serial architecture but are actuated remotely by motors fixed to the base with cables as transmission elements (see Fig. 1). Hence, we expect them to have the advantage of a large workspace like serial manipulators, while having a smaller moving mass and lower energy requirements like parallel manipulators. Additionally, they are also equipped with springs for stability and are actuated redundantly with more cables than their degree-of-freedom (DoF).

These manipulators are referred to as "tensegrity-inspired manipulators" because they share certain similarities with the authentic tensegrity systems presented in, e.g., [2]. Firstly, all their elements (bars, cables, springs) are loaded axially, i.e., in tension or compression. Secondly, they are inherently stable due to the springs. Thirdly, it is possible to modify their stiffness at a given configuration by changing the tension in the redundant actuating cables, akin to the prestressability of tensegrity structures. However, there are also a few differences with the conventional tensegrity systems, in that, the rigid bodies are not isolated from one another in the manipulator, and there are certain bars loaded in tension whose replacement with cables is potentially possible. Since three of the five fundamental properties of tensegrity systems are respected, the manipulators considered in this work are called tensegrity-inspired manipulators. A more detailed discussion on this topic can be found in [3],[4].

One of the research directions in the study of robot manipulators is their design optimization. A comprehensive review of performance measures and optimization of parallel manipulators has been presented in [5]. One of the interesting design problems is to optimize the dimensions of a manipulator so that its workspace is as close as possible to a user-prescribed workspace [6]. Another variant of the problem involves the optimal design of a manipulator for good dynamic performance while it is constrained to possess at least a user-prescribed region inside its workspace [7]. Inspired by these problems, the goal of the present work is to perform design optimization of the tensegrity-inspired manipulators presented in Fig. 1. Before discussing the specific challenges involved in this problem, a brief overview of the applications of tensegrity-type robots is presented in the following.

Since tensegrity systems closely resemble the musculoskeletal scheme in the vertebrates, they are widely used for developing biomimetic systems, e.g., bird's neck in [8], elephant's trunk in [9]. The high stiffness-to-mass ratio of tensegrity systems has promoted their use in locomotion systems [10],[11]. More applications of tensegrity systems can be found in [12].

The current literature on the optimal design of tensegrity-type systems is rather limited. In a recent study [13], the parameters of a tensegrity-based robot have been optimized to achieve energy efficiency over a desired trajectory using the concept of eigenmotion. It was noted that the large number of components (i.e., springs and bars) in these systems provide many design variables that can leveraged to achieve the desired characteristics in them.

A piping inspection robot with 4-SPS-U tensegrity joints has been considered in [14]. Each joint consists of a universal coupling between the base and top platforms and contains four springs on the sides, with a cable passing through each for actuation. A design optimization problem has been solved by considering the height of the joint and the free length of the springs as optimization variables to maximize the stiffness of the joint at the zero orientation (i.e. when the base and top platforms are parallel to each other). All the other parameters, such as the joint width and stiffness of the springs, were determined a priori based on other practical considerations. It must be noted that gravity effects were neglected in their work, and the actuators were used as a force source to impose the tension in cables in an open-loop control scheme. Thus, in the potential energy formulation and, subsequently, in the equilibrium equations and stiffness matrix, both spring parameters and cable tensions appear.

Another study concerns the design of tensegrity-based manipulators respecting the remote center of motion constraint for a medical application [15]. Two variants of the X-shaped tensegrity mechanism inspired by the Snelson's tensegrity structure (see [16]) are considered. The first one contains two actuated crossed bars and springs on all four sides for stability. The second one, in contrast, has crossed bars of fixed length, springs on the top and bottom for stability, and two cables on the sides for actuation. In design approach 1, the first and second joints are stacked in series to form a tensegrity-based manipulator. On the other hand, in design approach 2, two of the second joints are stacked in series to form a different tensegrity-based manipulator. The orientation limits and distance from the remote center of motion are studied for the two manipulators for different ranges of movements of the actuators. This study helps select a suitable actuator for the two manipulators. But, there is still scope for optimization, considering the bar lengths (for the second joint) and the free length of the springs. This problem has been addressed in [17], where the authors perform optimization of the first manipulator proposed in [15] for compactness. They consider the lengths of the bars, the free length of springs, and the displacement bounds of the actuators as design variables to find the optimal manipulator design that reaches a prescribed workspace. However, we note that both of these works neglect the gravity effects and use actuators as a positon source for fixing the position of some nodes (attachment points between components) with a closed-loop control scheme. Consequently, the potential energy of the manipulator is only due to the elasticity of the springs. Further, since they use identical springs at all locations, the spring stiffness factors out in the expression of potential energy and only scales the stiffness of the manipulator without any influence on the equilibrium equations. Thus, the spring stiffness was not included as a design variable in [15],[17].

This paper addresses the problem of design optimization for tensegrity-inspired manipulators displayed in Fig. 1 for a prescribed workspace while carrying a given point mass payload at the end-effector. The four cables indicated in colors[1] (see Fig. 1) are used to impose forces in the connecting nodes in an open-loop control scheme as in [14]. But, unlike in previous studies [14][15],[17], gravity plays a significant role in this problem, which complicates the model significantly. While

[1]For interpretation of the references to color, the reader is referred to the web version of this article.

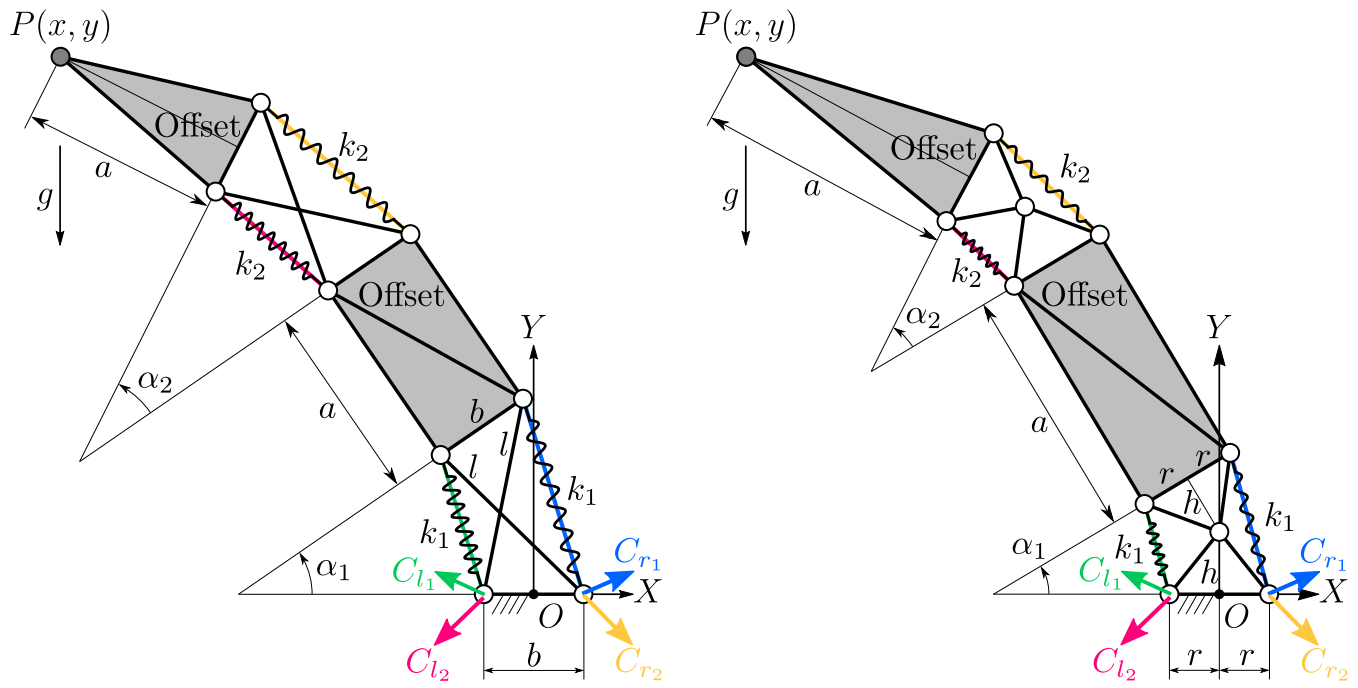

(a) 2-X manipulator

(b) 2-R manipulator

Figure 1: Schematics of the manipulators under study: 2-X (left) and 2-R (right).

the workspace of conventional manipulators is determined solely by kinematic factors (singularities, joint limits, link interferences), the workspace of tensegrity-inspired manipulators is further qualified by static factors (wrench-feasibility and stability). Thus, an optimal design of this class of manipulators for a given workspace must consider several additional design variables, e.g., the parameters of springs, masses of the constituent bars, etc. This makes the design problem more challenging than those of the conventional manipulators.

While designing the manipulators for a desired workspace, they will be optimized to achieve minimum actuation force, moving mass, and size. These objectives are global performance measures that do not depend on the configuration of the manipulator. Hence, the resulting optimal designs will be generally "good" for all tasks but may not be the best choice for any particular task. It is also possible to conduct the design optimization by considering configuration-dependent local measures of the manipulator, such as dexterity indices for good velocity performance, force application capabilities, stiffness measures, or even dynamic parameters like eigenfrequency. However, the resulting optimal design is likely to be best suited only for the optimized task and a poor one for others. Since we do not have specific information about the intended use of these manipulators, the scope of this paper will be limited to design optimization considering only the global performance measures, namely, workspace, actuation force, mass, and size.

A similar study has been conducted for 1-DoF X and R joints equipped with zero free length springs and actuated antagonistically by two cables on the sides, in [18]. However, an extension of that study to 2-DoF manipulators is accompanied by several challenges. Firstly, realizing the zero free length assumption for the springs in joints that are not fixed to the ground is extremely difficult. Thus, the hypothesis of "zero free length" for the springs has been relaxed and a new optimization variable has been added. Secondly, the cables must be routed along the bars of the first joint appropriately to actuate the second one independently. This routing, along with the springs and payload, will induce significant loads in the bars. Hence, it is also necessary to ensure that the bars are well-designed to withstand these loads. Finally, the workspace of the manipulators is two-dimensional, which makes their quantification and comparison more complex than those of the single joints. All of these challenges have been addressed in [1] for a given design of these manipulators. Building on that work, we perform the design optimization and comparison of these two manipulators in this article. The main contributions of this study may be summarized as follows:

- Two tensegrity-inspired manipulators with two anti-parallelogram and revolute joints, respectively, are optimized for their maximal actuation force, mass, and size for a specified payload and a desired workspace in the form of a disk.
- The Pareto optimal fronts are obtained using a genetic algorithm-based optimizer for the two manipulators, and optimal designs are compared from them.
- Several payload and workspace disk specifications are considered to characterize the two manipulators in terms of (moving mass/payload) and (size/disk radius) metrics.

The design optimization of the 2-DoF manipulators considered in this work is of significant relevance even for the development of manipulators with higher DoF. This is because the optimized 2-DoF chain can be used as a building block to develop more sophisticated manipulators. For instance, it is possible to add a third actuator at the end-effector point P (see Fig. 1) to conceive a planar manipulator with all 3-DoF without affecting the model of the first two joints. Similarly, the 2-DoF chain can be placed on a large rotating base to create a spatial 3-DoF manipulator for positioning tasks. It is also possible to add a 3-DoF spherical wrist with embedded actuators at the end-effector point of the 3-DoF spatial positioning manipulator to create a 6-DoF manipulator. In all the variants discussed above, the 2-DoF arm can be decoupled from the rest of the manipulator and its design optimization can be conducted separately.

The rest of this paper is organized as follows: the architecture of 2-X and 2-R tensegrity-inspired manipulators, their static model, and workspace are presented in Section 2. The design variables and their bounds are defined for the two manipulators in Section 3. The radius of the maximal inscribed disk in the workspace is maximized for different payloads in Section 4. The force, mass, and size optimization problem for a specified payload and workspace disk is posed and solved in Section 5. The same problem is solved for different payload and disk radius specifications in Section 6. Then, potential applications and extensions of the proposed design scheme are discussed in Section 7. Finally, the conclusions of this work are presented in Section 8.

2 Architecture of the two manipulators and their workspace

The 2-X and 2-R tensegrity-inspired manipulators are described in section 2.1, their static model is presented in Section 2.2, and their joint space and workspace are presented in Section 2.3.

2.1 Description of the manipulators

The schematics of 2-X and 2-R manipulators, are shown in Figs. 1(a) (left) and 1(b) (right), respectively. They are each a 2-DoF robotic system used to control the position of an end-effector point $P(x, y)$, containing a point payload of mass m_{p}.

The 2-X manipulator is composed of two X-joints arranged in series with rigid offsets (highlighted in shading) as shown in Fig. 1(a). Each X-joint consists of a top bar and a base bar of length b, and two crossed bars of length l, satisfying the condition $(l > b)$ for its assembly. All the bars are connected to their neighbors with pivots.

On the other hand, the 2-R manipulator contains R-joints instead of X-joints, with the same arrangement of offsets, as illustrated in Fig. 1(b). An R-joint is made of two congruent isosceles triangles (each composed of three bars), one inverted on top of the other. The semi-base length r and height h specify the geometry of these triangles.

In both manipulators, for joint i, the orientation of the top bar relative to its base is denoted by α_i, with $i = 1, 2$, as shown in Fig. 1. The joint i is equipped with two identical extension springs of stiffness k_i and free length l_{0_i}, on either side to ensure that the manipulator remains in stable equilibrium at the home configuration $(\alpha_1, \alpha_2) = (0, 0)$ rad[2] when no external or actuation forces are applied. In both manipulators, there exist two rigid offsets (in the form of trusses) of length a between the two joints and between the second joint and the end-effector point P, as indicated by the shaded portions in Fig. 1. Note that the purpose of shading is only to differentiate between the offsets and joints, while both are composed of bars and pivots. All the bars and springs are arranged in parallel planes to avoid any interference between them. This arrangement also provides improved rigidity for these manipulators in the direction normal to the plane of movement, as is necessary for their practical realization. All the bars are assumed to be inelastic in this study.

The manipulators are placed such that their plane of motion is parallel to the direction of gravity (see Fig. 1), which ensures that there is only a transmission of axial forces between the constituent elements. In order to preserve this property and keep the moving structure light, these manipulators are actuated *remotely* by motors installed on the ground, using cables as transmission elements. Each joint is actuated by two cables antagonistically as shown in Fig. 1. The cables actuating the second joint are routed through the rigid bars of the first joint and offset to achieve independence in actuation. This routing is not shown explicitly in Fig. 1 for the sake of visual clarity, but can be found in D. The cables are assumed to be massless and inelastic. The forces in all the cables are considered to be bounded by $F_{\min}$ and $F_{\max}$, with $F_{\min} = 0$ N for simplicity. All the pulleys that enable routing of cables are assumed to have zero radii in the model for ease of computation. In order to justify this assumption, it has been shown in D that incorporating the actual radius of the pulley does not alter the static model or the workspace of the manipulator significantly.

The visible difference between the two architectures is that for the 2-R manipulator, the two instant centers of rotation are located at the "central" pivots of the R-joints, while for the 2-X manipulator, the centers of rotations are not at fixed pivots but at the virtual intersection of diagonal bars of the X-joints. The hidden difference is that the antagonistic cable actuation increases (resp. decreases) the stiffness of the 2-X manipulator (resp. 2-R manipulator), as in the case of single X- and R-joints explained in [18].

[2]In this paper, all the angular parameters are presented in radians unless specified otherwise.

The static model of the manipulators is briefly described in the following.

2.2 Static model of the manipulators

The total potential energy of the manipulator can be expressed as follows:

$$U = U_{\text{gk}} + F_{l_1} l_{l_1} + F_{r_1} l_{r_1} + F_{l_2} l_{l_2} + F_{r_2} l_{r_2} \tag{1}$$

where U_{gk} accounts for the potential energy associated with gravity and springs, F_{l_i}, F_{r_i} represent the forces imparted by the cables C_{l_i}, C_{r_i}, respectively, and $l_{l_i}(\alpha_i), l_{r_i}(\alpha_i)$ represent the varying lengths of the cables C_{l_i}, C_{r_i}, respectively, for $i = 1, 2$.

The static equilibrium equations of the manipulator can be derived by differentiating U w.r.t. α_1 and α_2, as follows:

$$\begin{cases} \frac{\partial U}{\partial \alpha_1} := \frac{\partial U_{\text{gk}}}{\partial \alpha_1} + F_{l_1} \frac{\mathrm{d} l_{l_1}}{\mathrm{d} \alpha_1} + F_{r_1} \frac{\mathrm{d} l_{r_1}}{\mathrm{d} \alpha_1} = 0 \\ \frac{\partial U}{\partial \alpha_2} := \frac{\partial U_{\text{gk}}}{\partial \alpha_2} + F_{l_2} \frac{\mathrm{d} l_{l_2}}{\mathrm{d} \alpha_2} + F_{r_2} \frac{\mathrm{d} l_{r_2}}{\mathrm{d} \alpha_2} = 0 \end{cases} \tag{2}$$

A configuration (α_1, α_2) of the manipulator is said to be wrench-feasible if the static equilibrium equations can be satisfied while respecting the bounds on the actuation forces, i.e., $F_{l_i}, F_{r_i} \in [F_{\min}, F_{\max}]$, for $i = 1, 2$. The set of all (α_1, α_2) coordinates that are wrench-feasible forms the wrench-feasible joint space of the manipulator.

The stiffness matrix of the manipulator can be derived by computing the Hessian of the potential energy w.r.t. (α_1, α_2) as follows:

$$\mathbf{K} = \begin{bmatrix} K_{11} & K_{12} \\ K_{12} & K_{22} \end{bmatrix}, \text{ where } \begin{cases} K_{11} = \frac{\partial^2 U_{\text{gk}}}{\partial \alpha_1^2} + F_{l_1} \frac{\mathrm{d}^2 l_{l_1}}{\mathrm{d} \alpha_1^2} + F_{r_1} \frac{\mathrm{d}^2 l_{r_1}}{\mathrm{d} \alpha_1^2} \\ K_{22} = \frac{\partial^2 U_{\text{gk}}}{\partial \alpha_2^2} + F_{l_2} \frac{\mathrm{d}^2 l_{l_2}}{\mathrm{d} \alpha_2^2} + F_{r_2} \frac{\mathrm{d}^2 l_{r_2}}{\mathrm{d} \alpha_2^2} \\ K_{12} = \frac{\partial^2 U_{\text{gk}}}{\partial \alpha_1 \partial \alpha_2} \end{cases} \tag{3}$$

An equilibrium configuration (α_1, α_2) is said to be stable if the matrix $\mathbf{K}(\alpha_1, \alpha_2)$ can be made positive definite for at least one combination of actuation forces $F_{l_1}, F_{r_1}, F_{l_2}, F_{r_2} \in [F_{\min}, F_{\max}]$. Since there are two equilibrium equations and four actuation forces, there is an actuation redundancy of order two. This redundancy can be exploited to achieve different stiffnesses for the manipulator at a given configuration (α_1, α_2), i.e., exhibit variable stiffness.

The set of all (α_1, α_2) coordinates where the conditions of wrench-feasibility, as well as stability, are met forms the stable wrench-feasible joint space (SWFJ) of the manipulator. Further, the map of SWFJ onto the task space using the direct kinematic model produces the stable wrench-feasible workspace (SWFW) of the manipulator.

The SWFJ and SWFW are illustrated with an example in the next section.

2.3 Illustration of the SWFJ and SWFW

This section briefly presents the computation method and the important features of the SWFJ and SWFW of the two manipulators. As a numerical illustration, let us consider a 2-X manipulator with the following parameters: $b = 0.1492$ m, $l = 0.2996$ m, $a = 0.2693$ m, $k_1 = 2542.8877$ N/m, $l_{0_1} = 0.2038$ m, $k_2 = 749.1274$ N/m, $l_{0_2} = 0.1576$ m, $F_{\max} = 175.9986$ N. These parameters have been adopted from the design X_{IV} in Table 6, where the other parameters such as bar cross-sections can also be found. The derivation of this design and its properties will be explained in detail in later sections. In this section, it is only used to illustrate the SWFJ and SWFW of the manipulator.

The construction of SWFJ and SWFW is briefly described in the following. The reader is referred to [1],[19],[20] for more details.

1. Determine the joint limits $\alpha_i = [-\alpha_{\max_i}, \alpha_{\max_i}]$ for joint $i = 1, 2$, based on the free length l_{0_i} of the springs installed in them. For the above example, $\alpha_{\max_1} = 0.8818$ rad, $\alpha_{\max_2} = 2.1279$ rad.
2. Discretize the joint space into 50 equally spaced vertical (resp. horizontal) grid lines along the α_1 (resp. α_2) axis within the joint limits.
3. Determine the feasible (i.e., wrench-feasible and stable) intervals in each grid line (i.e., for a given value of α_1 or α_2) by rewriting limiting conditions of wrench-feasibility and stability as univariate polynomials and solving them accurately. The limiting points of the feasible intervals represent the boundary of the SWFJ. Thus, in general, we have 200 points (two points on each grid line) on the SWFJ boundary.
4. Perform a linear interpolation between the successive limiting points to obtain a polygonal approximation of the SWFJ.
5. Plot the singularities of the manipulator inside the SWFJ and perform a linear interpolation between them.

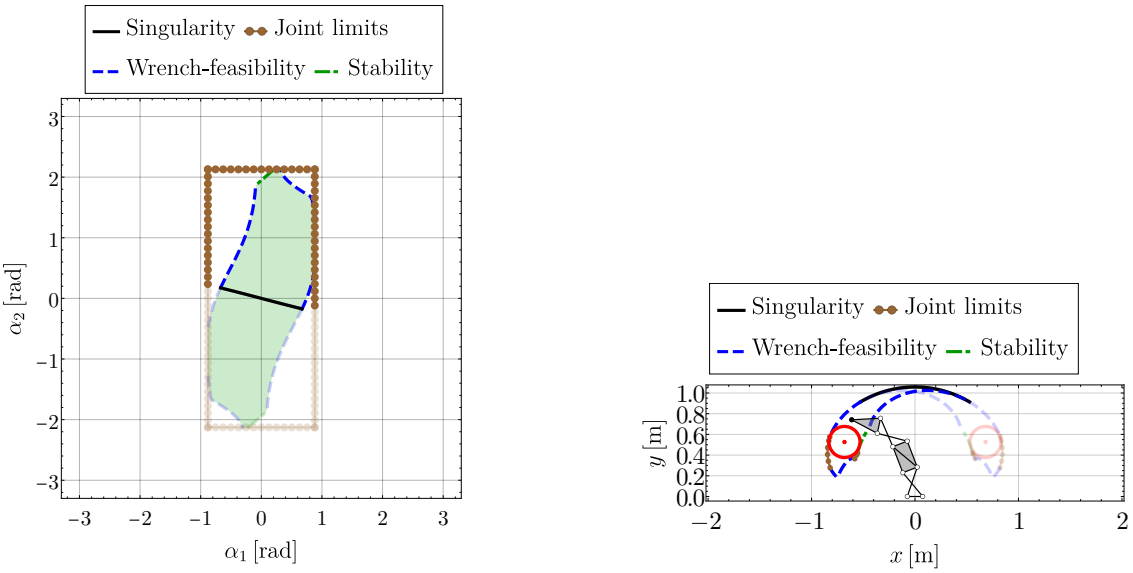

(a) SWFJ (b) SWFW

Figure 2: Stable wrench-feasible joint space (SWFJ) and stable wrench-feasible workspace (SWFW) for the 2-X manipulator with: $b = 0.1492$ m, $l = 0.2996$ m, $a = 0.2693$ m, $k_1 = 2542.8877$ N/m, $l_{0_1} = 0.2038$ m, $k_2 = 749.1274$ N/m, $l_{0_2} = 0.1576$ m, $F_{\max} = 175.9986$ N. The bounding curves of the SWFJ are formed by joint limits (bubbles), wrench-feasibility condition (equal dashed lines), and stability condition (unequal dashed lines). The SWFJ region is highlighted by shading and the singularity (continuous line) of the 2-X manipulator is plotted inside it. Inside the SWFJ, the boundaries lying above the singularity curve are shown in opaque style and those below it are shown in transparent style. The images of these curves in the task space are also shown in the same style to enable correspondence between them. Two maximal disks with a radius of 0.15 m each have been inscribed inside the SWFW.

6. Map the polygonal boundary of SWFJ and the singularity onto the task space using the direct kinematic model to obtain a polygonal approximation of the SWFW.

Following the above steps, the SWFJ and SWFW of the 2-X manipulator have been plotted in Figs. 2(a) and 2(b), respectively. After determining the SWFJ boundary points, they were classified based on their limiting conditions into joint limits, wrench-feasibility, and stability to gain more insight into the boundaries. In the plots, the respective sides of the polygons connecting these points are shown in different styles: joint limits (bubbles), wrench-feasibility (equal dashed lines), and stability (unequal dashed lines). Finally, the singularity curve has been plotted inside the SWFJ polygon in a continuous style. It is observed that the singularity curve splits the SWFJ into two symmetric halves. All the boundaries that lie above this curve are shown in opaque style, while the ones that are below it are shown in transparent style. The images of these boundaries in the task space are also shown in the same style in Fig. 2(b) to enable correspondence between them. It is observed that the SWFW is composed of two overlapping parts that are symmetric about the y-axis. The symmetry in the joint space and the task space is a consequence of the symmetry in the architectures of the manipulator, its placement w.r.t. gravity, and its actuation schemes, about the home configuration $(\alpha_1, \alpha_2) = (0, 0)$, as inferred from Fig. 1.

It is important to note that since the SWFJ remains a single component, the manipulator can move between the two halves of the SWFJ crossing the singularity curve. In the task space, this amounts to moving from one connected part of the workspace to another by changing its posture at a singular configuration. This connectivity between the two parts is a desirable feature in the design of such manipulators. It can be achieved by enforcing a singular configuration to be inside the SWFJ. Since we know that at the home configuration $(\alpha_1, \alpha_2) = (0, 0)$, the instantaneous centers of rotation of the two joints as well as the end-effector point fall on the y-axis, it is a singular configuration for all dimensions of the two manipulators. Hence, the designer could specify the home configuration to be inside the SWFJ to ensure connectivity between the two halves of the SWFW.

Once the SWFW is derived, it is necessary to quantify it to be able to compare different designs of the manipulator. One possibility is to consider the surface area of the SWFW. However, this quantification cannot distinguish between a regularly shaped workspace and a thin long strip with equal area. Practically, a regular workspace is of greater interest to the designer as it is more suitable for a wide variety of tasks. For instance, it might represent the region inside which a product may be placed for inspection. From this perspective, it is also meaningful to quantify the workspace by inscribing a regular shape inside it and evaluating its dimensions. Several research works have followed this approach, e.g., the rectangle was used in [21], and the disk was considered in [22]. Inspired by these studies, we shall consider the maximal inscribed disk to quantify the workspace, even though it may not represent the actual shape of the workspace. Since the SWFW is in the form of polygons, an open-source `c++` library `polylabel` has been used to find the maximally inscribed disk(s) ($\mathcal{D}$) inside it[3]. The tolerance in computing the disk center and radius is set at 10^{-5} m. For the example presented in Fig. 2(b), the inscribed disks in the SWFW have a radius

[3]The associated code can be found at `https://github.com/mapbox/polylabel`.

of 0.15 m each. It is noted that this study only measures the size of the maximally inscribed disk without any regard for its placement in the SWFW. In general, this would not be an issue since the base of the manipulator or the workstation(s) can be adjusted suitably to position the workpiece inside the disk. The radius of this disk, denoted by r_{d}, will be used as a measure of the size of the SWFW for these manipulators. This maximal inscribed disk will be referred to as the "SWFW disk" in the following. The computation of the SWFW disk starting from the static model takes only about 43 ms for the 2-X manipulator and 7 ms for the 2-R manipulator.

In [8], trajectory-tracking experiments were conducted on a very similar planar 3-X manipulator inside its theoretical wrench-feasible workspace. The tracking results were very good indicating that the model was accurate enough to the actual prototype. Since the manipulators considered in this study are also modeled similarly and their prototypes will also have the same components, we expect that the theoretical results derived in this work will also be close to the actual manipulator.

The eventual goal of this study is to conduct design optimization of the 2-X and 2-R manipulators, such that they contain the same SWFW disk ($\mathcal{D}(r_{\mathrm{d}})$) while carrying a point payload of mass m_{p}. In this regard, all the parameters that influence the SWFW of the two manipulators are identified and listed as design variables in the following section.

3 Design variables and their bounds

Table 1: Design variables and their bounds for the 2-X and 2-R manipulators. The brackets "[ ]" represent a closed interval while "] [" represent an open interval.

	2-X manipulator			**2-R manipulator**	
No.	Variable	Bounds		Variable	Bounds
1	b [m]	[0.05,1]		r [m]	[0.025,0.5]
2	$\lambda(l/b)$	]1,10]		$\mu(h/r)$	]0,5]
3	$\epsilon(a/b)$	]0,10]		$\epsilon(a/(2r))$	]0,10]
4	σ_α	]0,1[		σ_α	]0,1[
5	k_1 [N/m]	[0,10000]		k_1 [N/m]	[0,10000]
6	σ_{k_1}	[0,1]		σ_{k_1}	[0,1]
7	k_2 [N/m]	[0,10000]		k_2 [N/m]	[0,10000]
8	σ_{k_2}	[0,1]		σ_{k_2}	[0,1]
9	$F_{\max}$ [N]	[0,500]		$F_{\max}$ [N]	[0,500]

A set of nine design variables $\boldsymbol{u} = [u_1, \ldots, u_9]^\top$ has been presented for the two manipulators in Table 1. The first three define the geometry of the manipulators; the next one specifies the safe joint limits; the next four define the springs in the two joints; the last variable specifies the maximum force in the actuation cables. More details on these variables are presented in the following:

- **Variables 1-3 (Geometry)**: For the 2-X manipulator (resp. 2-R manipulator), all the bar lengths are defined by the variables (b, l, a) (resp. (r, h, a)). However, only the first variable, which signifies the width of the manipulator, has been used as is. The other two lengths have been embedded as ratios relative to the base. Thus, the first variable scales the entire manipulator while the other two determine the relative lengths of the bars. The limiting values for the width have been specified as $[0.05, 1]$ m for both manipulators (note that r represents half the width of the 2-R manipulator). The lower bound is necessary to overcome fabrication issues associated with small bars, while the upper bound has been set at 1 m to avoid extremely large manipulators. The lower bound for $\lambda(l/b)$ is set as 1 to respect the assembly condition for the X-joint. The limits for the other variables ensure that there is a reasonable ratio between the width and height of the manipulators. In addition, equivalent limits are set for the two manipulators so that they have nearly the same geometric space.

- **Variable 4 (Safe joint limit)**: The movement of the joints in 2-X and 2-R manipulators is limited due to their geometry and/or remote actuation by cables. For instance, the amplitude of movement of the X-joint is limited by the occurrence of flat singularity at $\alpha_i = \pi$. On the other hand, the movement of the R-joint is limited by the coincidence of the attachment points of the cables or collinearity of the cable with the joint center of rotation, depending on the geometry (r, h) of the joint [1]. In these cases, it is a practical necessity to remain *sufficiently* distant from these limiting configurations. But, the value for this distance is not an obvious one. Hence, a fraction (σ_α) is introduced as a design variable to define safe limits for joint movement. For the X-joint, while π represents the upper limit of the joint movement due to flat singularities, $\overline{\alpha_{\max}} = \sigma_\alpha \pi$ represents a safe upper bound for the movement of that joint. Similarly, for the R-joint, while $\overline{\overline{\alpha_{\max}}}$ represents the upper limit due to cable actuation, $\overline{\alpha_{\max}} = \sigma_\alpha \overline{\overline{\alpha_{\max}}}$ represents safe upper limit for that joint. More details on the joint limits of the two joints can be found in [1].

  It is further noted that the actual upper limit $(\alpha_{\max_i})$ of movement for joint i can be less than or equal to its safe limit $(\overline{\alpha_{\max}})$ depending on the free length (l_{0_i}) of the springs installed on that joint. From [1], it is recalled that the springs that prevent the joints from reaching their safe limits belong to set $\boldsymbol{\chi}_a$, while those which allow them to reach their safe limits belong to set $\boldsymbol{\chi}_b$. The set of all feasible springs is formed by $\boldsymbol{\chi}_a \cup \boldsymbol{\chi}_b$.

- **Variables 5-8 (Springs)**: Using the geometry and safe joint limits, the complete feasible space $(\boldsymbol{\chi}_a \cup \boldsymbol{\chi}_b)$ for the springs can be defined. This process has been illustrated in A. All the springs are assumed to be made of a standard material EN 10720-1 (SH/DH) (equivalently ASTM A228), whose shear modulus (G_k) is 81.5 GPa and volumetric density (ρ_k) is 7850 kg/m^3. The choice of spring for each joint i depends on the stiffness (k_i) and the spring selection parameter (σ_{k_i}) (see A for details). In order to ensure physical feasibility, the maximum stiffness value is set at 10000 N/m. Using (k_i, σ_{k_i}), all the other parameters of the spring: wire diameter (d), coil diameter (D), number of active coils (N_a), free length (l_{0_i}), and mass (m_{k_i}) can be computed. Further, based on the free length and the safe joint limit $(\overline{\alpha_{\max}})$, the maximum operating length $(l_{\max_i})$ of the spring can also be computed (see [1] for more details).
- **Variable 9 (Actuation force)**: The maximum actuation force $(F_{\max})$ of the cables is bounded inside $[0, 500]$ N for both the manipulators. The maximum bound is less than the rupture limit of commonly available synthetic cables, e.g., VECT070LE. This variable indicates the size of the motor required to actuate the manipulator.

In addition to the above variables, the SWFW is also affected by the mass of constituent bars of the manipulators. However, the cross-section and mass of the bars are not explicitly considered as design variables. Their values are determined from the limiting condition of buckling using the data of bar lengths, springs, and joint limits. The details of these computations are presented with an example for the two manipulators in [1]. All the bars are assumed to have a uniform circular cross-section with a radius ≥ 5 mm made of Aluminum material whose volumetric density is $\rho = 2700$ kg/m^3 and Young's modulus is $E = 70$ GPa.

The bounds in Table 1 define the design space for the two manipulators. The brackets "[ ]" represent a closed interval while "] [" represent an open interval. The next task is to formulate design optimization problems for the two manipulators with a constraint that they contain a specified disk inscribed inside their SWFW. However, at this point, it is not clear what disk size suits both manipulators. Moreover, it can also change depending on the payload (m_{p}) loaded at the end-effector. Hence, firstly, a study should be conducted on the feasible disk sizes for a given payload for the two manipulators. This analysis is carried out in the next section by posing design optimization problems to maximize the SWFW disk radius.

4 Workspace optimization for a given payload

In this section, the 2-X and 2-R manipulators will be designed to maximize the radius of the SWFW disk, while ensuring that the home configuration $(\alpha_1, \alpha_2) = (0, 0)$ is stable in the absence of actuation forces. The problem formulation is discussed in Section 4.1, the solution method in Section 4.2, and the results in Section 4.3.

4.1 Problem formulation

The optimization problem for maximizing the SWFW disk radius (r_{d}) while the manipulator carries a payload of mass m_{p} is posed as follows:

$$\begin{aligned} \underset{\boldsymbol{u}}{\text{Maximize}} \quad & r_{\mathrm{d}} \\ \text{subject to} \quad & \text{Stability at } (\alpha_1, \alpha_2) = (0, 0) \text{ with no actuation forces} \\ & u_i \in \left[\underline{u_i}, \overline{u_i}\right], \quad i = 1, \ldots, 9, \end{aligned} \tag{4}$$

where u_i refers to the i^{th} design variable listed in Table 1, and $\left[\underline{u_i}, \overline{u_i}\right]$ its lower and upper bounds, respectively, for both 2-X and 2-R manipulators. The stability at home configuration is imposed as a constraint for two reasons. Firstly, it is to ensure that the manipulators can stand on their own safely, without falling down, even when the motors are not powered. Secondly, it is to ensure that the manipulator can move between the two symmetric regions of the SWFW as explained in Section 2.3.

Note that the payload mass (m_{p}) does not appear explicitly in the above formulation. But, it is an implicit parameter that affects the SWFW directly through the static model and indirectly through the cross-sections of the bars [1].

The above problem is solved using an evolutionary optimization solver, as explained in the next section.

4.2 Genetic algorithm based solver: NSGA-II

In the optimization problem posed in Eq. (4), the computation of the objective function from a given set of design variables goes through several numerical steps, as illustrated in Section 2.3. Hence, gradient-based optimization methods cannot be used for the problem at hand. Also, it is tough for the designer to come up with an initial guess that is firstly feasible and secondly good enough. This issue is evident from the arbitrarily chosen example designs in [1], where the size of the manipulator is 20-200 times larger than the radius of the SWFW disk. Hence, a possible solution is to use evolutionary optimization algorithms, which require neither a good initial guess nor gradient information. Additionally, they explore the design space using heuristic operations that prevent stagnation around local optima. In this work, a genetic algorithm-based multi-objective evolutionary optimization tool, namely, `NSGA-II` (see [23]), will be used. The ability of this tool to handle multiple objectives has made

it attractive for design optimization of mechanisms [24], parallel manipulators [25], and robotic grippers [26], among others. The choice of NSGA-II in this work is motivated by the successful results on related problems, its widespread popularity, and finally, the access to the original code written by the authors[4]. It is remarked that there are also other multi-objective optimization algorithms, e.g., SPEA2 (see [27]), NSGA-III (see [28]), which could be suitable for the design problem at hand. However, a detailed exploration of all such methods is beyond the scope of this study.

Table 2: Internal parameters of the optimization solver NSGA-II along with their recommended and assumed values.

Parameter	**Recommended values**	**Assumed value**
Population size	Multiple of 4	5000
Number of generations	-	3000
Probability of crossover	[0.6, 1]	0.9
Probability of mutation	(1/no. of variables)	0.11
Distribution index for crossover	[5,20]	5
Distribution index for mutation	[5,50]	20
Seed for random number generator	[0,1]	0.3

There are a total of seven internal parameters in NSGA-II that the user must set to initiate an optimization run. They are listed along with their assumed values in Table 2. Large values have been chosen for the population size and the number of generations to enable a good exploration of the design space and a reasonably good convergence to the optimal solution. The probability of mutation is set to (1/number of design variables) as recommended in [23]. Most other parameters are adopted from another design problem presented in [7] with similar validations. However, the distribution index for mutation has been decreased from 35 in [7] to 20, to increase the variety of designs in subsequent generations. It has been verified through various trial runs that the results are not significantly impacted even while the parameters are changed within their prescribed bounds.

The parameters presented in Table 2 are used for all the design problems presented in this work for both 2-X and 2-R manipulators. It takes about 25 hours[5] for a design run of the 2-X manipulator, and about 6 hours for a design run of the 2-R manipulator.

The optimal SWFW disk radii obtained for different payloads are presented for the two manipulators in the next section.

4.3 Results and discussion

The problem posed in Eq. (4) has been solved for four different payloads $m_{\mathrm{p}} = \{0, 2, 5, 10\}$ kg at the end-effector, for the 2-X and 2-R manipulators. In the resulting optimal designs[6], it is observed that the design variable b (resp. r), which scales the 2-X manipulator (resp. 2-R manipulator), reaches its upper bound in most of the cases. In addition, the maximal actuation force $(F_{\max})$ also attains its upper bound of 500 N in all the cases. This shows that the optimal designs are as large as possible with maximum actuation forces to produce the largest SWFW disk, which is logical.

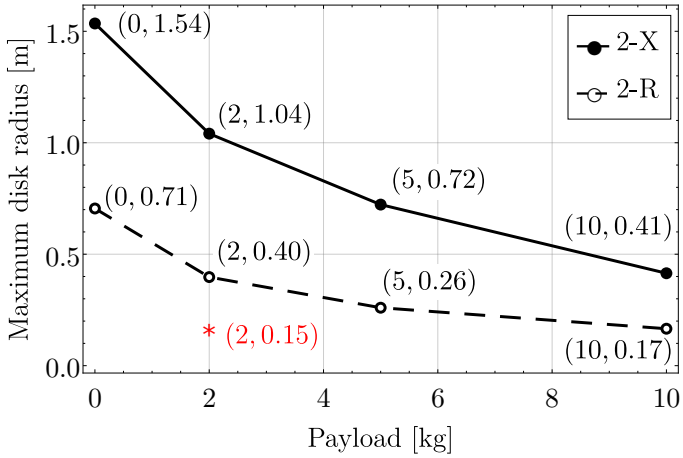

Figure 3: Maximum SWFW disk radius for different payloads at the end-effector.

The maximum SWFW disk radius (r_{d}) obtained for each payload is presented in Fig. 3. For both manipulators, it is found that the maximum disk radius decreases with the payload, which is logical. For all payloads, the SWFW disk radius for the 2-X

[4]The implementation of NSGA-II in C language can be found in https://www.egr.msu.edu/~kdeb/codes.shtml.

[5]All the computations reported in this work have been performed on a computer with an Intel® Core™ i7-6700 CPU running @ 3.40GHz processor, using a C++ code parallelized with OpenMP, employing eight threads.

[6]In this paper, the term "optimal design" is not used in the strict mathematical sense as the designs obtained through heuristic optimization algorithms cannot be proved for optimality.

manipulator is observed to be roughly two times greater than that of the 2-R manipulator. This result suggests that the 2-X manipulator should be preferred over its counterpart if the maximum SWFW disk size is the only criterion.

Additionally, the data in Fig. 3 can be used to find a feasible SWFW disk radius and payload specification that is sufficiently far from the limiting value for both manipulators. For instance, while the end-effector carries a 2 kg payload, both manipulators can have an SWFW disk radius of 0.15 m, as highlighted in Fig. 3. This information will be useful for further optimizing these manipulators in terms of their actuation force, moving mass, and size while fixing the same payload and SWFW disk radius for them. The following section performs this optimization.

5 Force, mass, and size optimization for a given payload and SWFW disk

This section aims to find "good" designs for the 2-X and 2-R manipulators capable of carrying a payload of 2 kg while possessing an SWFW disk of radius 0.15 m.

5.1 Formulation and resolution of the design problem

Three properties have been chosen to assess and compare the global performance of a design: the maximal actuation force, total moving mass (without payload), and size of the manipulator. Thus, a design optimization problem can be posed as follows:

$$\begin{aligned} \underset{\boldsymbol{u}}{\text{Minimize}} \quad & \begin{cases} \text{Force} : F_{\max} \\ \text{Mass} : \sum_{j=1}^{n_b} m_j + 2(m_{k_1} + m_{k_2}) \\ \text{Size} : y(\alpha_1 = 0, \alpha_2 = 0) \end{cases} \\ \text{subject to} \quad & \text{Stability at } (\alpha_1, \alpha_2) = (0,0) \text{ with no actuation forces} \\ & \mathcal{D}(r_{\mathrm{d}}) \in \text{SWFW}; \\ & u_i \in \left[\underline{u_i}, \overline{u_i}\right], \quad i = 1, \ldots, 9, \end{aligned} \tag{5}$$

where $F_{\max}$ is the maximum actuation force, which is also a design variable listed in Table 1, m_j represents the mass of the j^{th} moving bar, n_b is the total number of moving bars, m_{k_1}, m_{k_2} denote the masses of the springs installed in the first joint and second joint, respectively. The size of the two manipulators is quantified by their vertical reach at the home configuration, which is equivalent to the y-coordinate of the end-effector at the home configuration $(\alpha_1, \alpha_2) = (0,0)$.

The stability of the home configuration in the absence of actuation forces is imposed as a constraint as in the previous problem (see Eq. (4)). In addition, the maximal inscribed disk ($\mathcal{D}$) in the SWFW is prescribed to have a radius greater than or equal to a user-specified value r_{d}. Using the data from the previous section, disk radius $r_{\mathrm{d}} = 0.15$ m and the payload $m_{\mathrm{p}} = 2$ kg are set considering the feasibility for both the manipulators. Finally, the details on design variables u_i can be found in Table 1.

The above problem is solved in several stages using the `NSGA-II` solver, as explained in the following.

5.2 Solution method and the Pareto optimal front

Since there are three objectives in the optimization problem posed in Eq. (5), its complete solution will be formed by a 2-dimensional Pareto front in the objective space. The `NSGA-II` solver can handle multiple objectives to produce the desired solutions on the Pareto front. However, instead of using it directly on the above problem, it is used in two stages as illustrated in Fig. 4. The first one finds the extremal designs in the Pareto front, while the second one uses them to construct the Pareto front, as detailed in the following:

- Single objective optimization problems with force, mass, and size as objectives are solved separately. In these problems, the optimal design obtained while maximizing the SWFW disk size for a 2 kg payload (see Section 4.3) is added to the initial population since it is a known feasible design. This inclusion helps generate new feasible designs and better explore the feasible design space.
- A multi-objective optimization problem with force, mass, and size as three objectives is formulated. The three optimal designs obtained in the previous step are added to the initial population to aid the solver in producing a well-distributed Pareto front.

The Pareto fronts obtained for the 2-X and 2-R manipulators are shown in Figs. 5(a) and 5(b), respectively. It is observed that the Pareto front of the 2-X manipulator is spread over a much wider range along all three axes than that of the 2-R manipulator, indicating that it has a better diversity of optimal designs. Both Pareto fronts appear to have some discontinuities attributed to the constraints in the problem. It is also observed that both plots are extremely sparse near the lower bounding values of $F_{\max}$.

The extremal designs in the Pareto front of the two manipulators marked in Fig. 5 are studied in the next section, and several other compromise designs are presented in the subsequent section.

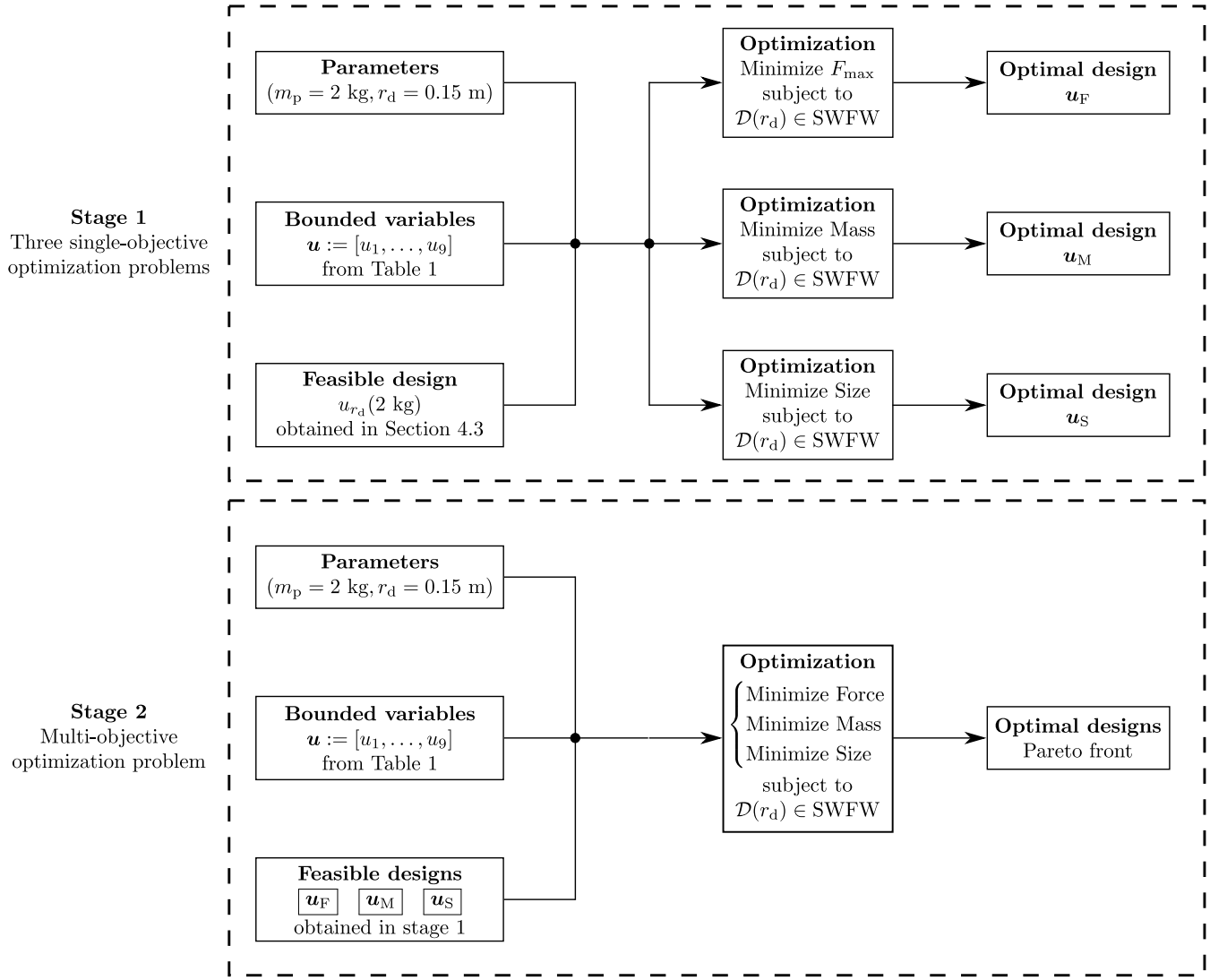

Figure 4: Design optimization in two stages to obtain a well-distributed Pareto front.

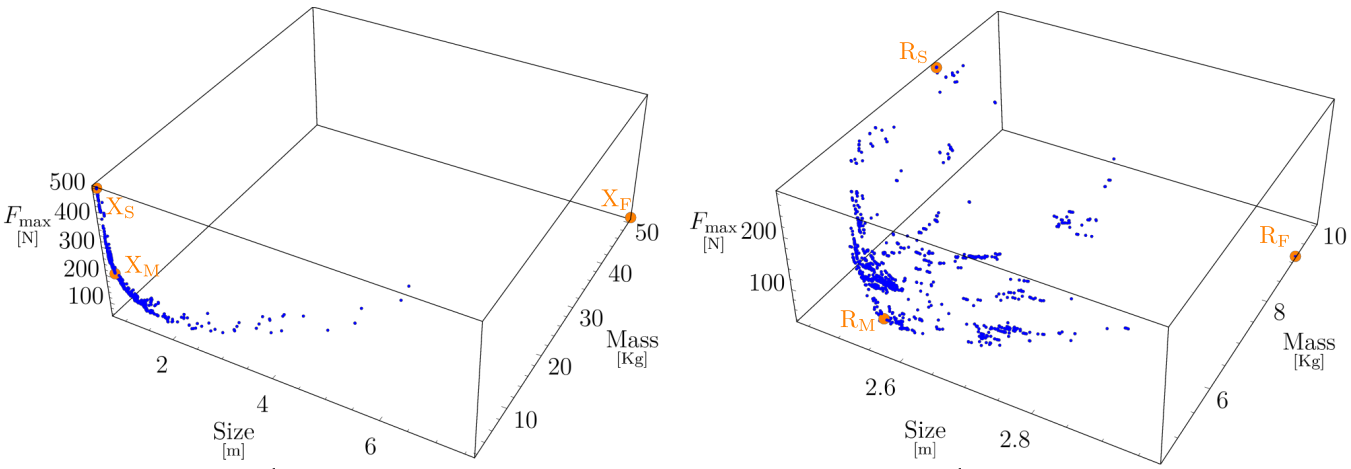

(a) 2-X manipulator
- $F_{max} \in [56.4474, 498.0113]$ N
- Mass $\in [1.4744, 50.8691]$ kg
- Size $\in [0.7648, 7.6679]$ m

(b) 2-R manipulator
- $F_{max} \in [38.5137, 275.1206]$ N
- Mass $\in [4.5659, 10.0591]$ kg
- Size $\in [2.4306, 2.9799]$ m

Figure 5: Pareto fronts for the two manipulators obtained for a payload (m_p) of 2 kg and SWFW disk of radius (r_d) 0.15 m.

5.3 Extremal designs on the Pareto front

The force, mass, and size optimal designs of the 2-X manipulator (resp. 2-R manipulator), denoted by X_F, X_M, X_S (resp. R_F, R_M, R_S), respectively, are presented in Table 3 (resp. Table 4). In addition to the values of the design variables, the dependent parameters are also presented below them in "{ }" for completeness. After the rows containing design variables, the actual limits of movement for the first and second joints are presented. This is followed by the six dependent spring parameters $(d, D, N_a, l_{0_i}, l_{\max_i}, m_{k_i})$ computed using the design variables k_i and σ_{k_i} for springs in the i^{th} joint. The designer can use these parameters directly for its fabrication. Then, the cross-section radii of the moving bars calculated implicitly using the other data are presented. Note that the bars are numbered from the bottom-left to the top-right (see [1] for more details). Finally, the three objectives (force, mass, size) are presented for all the designs, and the minimum value for each objective is highlighted with a box.

The manipulators corresponding to optimal designs and their SWFW are presented in Figs. 6, 7, 8 for a visual comparison. All the designs in this paper are presented on the same scale to make this comparison possible.

Using the data in Tables 3 and 4 and Figs. 6, 7, 8, the following observations are made on the force, mass, and size optimal designs of the two manipulators:

- **Objectives**: Generally, there is a strong compromise between the force and size values between the respective optimal designs for both manipulators. For the 2-X manipulator, between designs X_F and X_S, $F_{\max}$ increases from 56.4474 N to 495.6961 N to achieve a reduction in size from 7.6679 m to 0.7648 m. The mass optimal design X_M is placed in between with an $F_{\max}$ of 217.0522 N and a size of 0.9179 m. On the other hand, for the 2-R manipulator, between the designs R_F and R_S, $F_{\max}$ increases from 38.5137 N to 273.5630 N to achieve a reduction in size from 2.9799 m to 2.4306 m. The design R_M is placed between them with an $F_{\max}$ of 103.5777 N and a size of 2.5761 m.

- **All designs**: Some features are common in all the optimal designs of both manipulators. The inscribed SWFW disk has a radius that is marginally greater than the specified value of 0.15 m, as expected. The actual joint limit for the second joint is equal to the safe joint limit, i.e., $\alpha_{\max_2} = \overline{\alpha_{\max}}$, while it is lesser for the first joint. Firstly, this indicates that the first joint, which supports a more significant mass (first offset and second joint with its springs), moves over a shorter range than the second joint, which supports a smaller mass. Secondly, the fact that the second joint reaches its safe limits reveals that the springs in that joint belong to the set $\boldsymbol{\chi}_b$, i.e., springs with free length smaller than the critical distance between their attachment points at the safe joint limits. On the other hand, the springs in the first joint belong to the set $\boldsymbol{\chi}_a$, i.e., springs with a larger free length (see [1] for more details on this classification).

  The springs in the first joint are stiffer and have a longer free length (l_{0_i}) than the ones in the second joint. But, the springs in the second joint are wider (except in design X_S), i.e., have a larger coil diameter (D), and longer operating length $(l_{\max_i})$ than their counterparts.

- **Designs $\mathbf{X_F}, \mathbf{X_M}, \mathbf{X_S}$**: The design X_F is much taller (≈9 times), wider (≈7 times) and heavier (≈30 times) than X_M and X_S as presented in Fig. 6(a). Hence, it may not be preferred despite its smaller actuation force (≈1/7 times). On the other hand, the designs X_M and X_S are compact and have a moving mass that is smaller than the payload $(m_p = 2 \text{ kg})$ loaded at the end-effector, which makes them more attractive than X_F. Between X_M and X_S, the former would be a more reasonable choice owing to a smaller force requirement (≈1/2 times) and comparable mass and size values.

- **Designs $\mathbf{R_F}, \mathbf{R_M}, \mathbf{R_S}$**: In all the optimal designs of 2-R manipulator, it is observed that the ratio (h/r) is close to unity, which indicates that the R-joint tends to have a geometry that keeps the joint limit $(\overline{\alpha_{\max}})$ due to actuation cables close to its maximum value of $\frac{\pi}{2}$ (see [1]). Another point to be noted is that the ratio (h/r) is greater than one in all designs, contrary to what was observed for the optimal designs of a single R-joint in [18]. This difference is because of the free length (l_{0_i}) of the springs that were neglected in that study. It was proved in that work that $(r > h)$ is necessary to stabilize the R-joint when springs are of zero free length. But, with a non-zero free length for springs, we find that it is possible to stabilize the R-joint for other geometries as well, and furthermore, all the optimal designs of the 2-R manipulator are such that h is slightly greater than r.

  Unlike in the 2-X manipulator, the sizes of all three designs of the 2-R manipulator are comparable and are significantly larger than the specified SWFW disk radius. Despite the similarity in size, they have a significant difference in their forces and masses. The design R_S has a larger mass and higher force requirements for a marginally smaller size and is hence not a favorable one. However, between the designs R_F and R_M, there is no obvious choice. The former must be chosen if a smaller force is the priority, while the latter must be chosen if a smaller mass is the priority.

- **Designs $\mathbf{X_F}, \mathbf{R_F}$**: From Fig. 6, it is apparent that the design R_F has a smaller (≈ 1/1.5 times) $F_{\max}$ and is significantly better than X_F in terms of other two the objectives, and is hence a preferred choice as force optimal design.

- **Designs $\mathbf{X_M}, \mathbf{R_M}$**: From Fig. 7, it is observed that the design X_M has a smaller mass (≈1/3 times), smaller size (≈1/3 times) and a larger force requirement (≈2 times) when compared to the design R_M. Based on the mass value, it is clear that the design X_M should be preferred over R_M as the mass optimal design.

- **Designs $\mathbf{X_S}, \mathbf{R_S}$**: From Fig. 8, it is observed that the design X_S has a smaller mass (≈1/5 times), smaller size (≈1/3 times)

Table 3: Force, mass, and size optimal designs of the 2-X manipulator for carrying a payload of mass 2 kg and inscribing an SWFW disk of radius 0.15 m.

Variables	**Limits**	**Optimal designs**		
		$\mathrm{X_F}$	$\mathrm{X_M}$	$\mathrm{X_S}$
b [m]	$[0.05, 1.0]$	0.9209	0.1341	0.1193
$\lambda\,(l/b)$ $\{l$ [m]$\}$	$]1, 10]$	1.7553 $\{1.6165\}$	2.0275 $\{0.2720\}$	2.3865 $\{0.2846\}$
$\epsilon\,(a/b)$ $\{a$ [m]$\}$	$]0, 10]$	2.7205 $\{2.5054\}$	1.6574 $\{0.2223\}$	1.0392 $\{0.1239\}$
σ_α $\{\overline{\alpha_{\max}}$ [rad]$\}$	$]0, 1[$	0.7271 $\{2.2842\}$	0.7060 $\{2.2179\}$	0.8054 $\{2.5304\}$
k_1 [N/m]	$[0, 10000]$	2724.9509	2432.2837	1917.3040
σ_{k_1}	$[0, 1]$	0.9704	0.2736	0.7956
k_2 [N/m]	$[0, 10000]$	179.1459	834.2743	1169.9118
σ_{k_2}	$[0, 1]$	0.9586	1.0000	0.9902
$F_{\max}$ [N]	$[0, 500]$	56.4474	217.0522	495.6961
$\{\alpha_{\max_1}, \alpha_{\max_2}\}$ [rad]		$\{0.3586, 2.2842\}$	$\{1.1252, 2.2179\}$	$\{1.9170, 2.5304\}$
Spring 1: $\{d$ [mm], D [mm], N_a, l_{0_1} [m], $l_{\max_1}$ [m], m_{k_1} [kg]$\}$		{6.0, 29.60, 186.88, 1.17, 1.50, 3.92}	{3.4, 24.46, 38.27, 0.18, 0.32, 0.23}	{3.9, 34.90, 28.91, 0.18, 0.37, 0.33}
Spring 2: $\{d$ [mm], D [mm], N_a, l_{0_2} [m], $l_{\max_2}$ [m], m_{k_2} [kg]$\}$		{5.9, 111.73, 49.40, 0.51, 2.41, 3.95}	{3.2, 39.00, 21.59, 0.14, 0.39, 0.19}	{3.4, 33.56, 30.78, 0.17, 0.40, 0.25}
Bar cross-section radius r_{b_j} [mm] $j = 1, \ldots, 12$		{16.73, 16.73, 10.68, 18.13, 18.92, 18.13, 7.11, 9.14, 9.14, 5.50, 6.03, 6.03}	{6.41, 6.41, 5.00, 5.00, 5.17, 5.00, 5.00, 5.00, 5.00, 5.00, 5.00, 5.00}	{7.59, 7.59, 5.00, 5.00, 5.00, 5.00, 5.00, 5.00, 5.00, 5.00, 5.00, 5.00}
Mass [kg]		50.8691	1.4744	1.7860
Size [m]		7.6679	0.9179	0.7648

Table 4: Force, mass, and size optimal designs of the 2-R manipulator for carrying a payload of mass 2 kg and inscribing an SWFW disk of radius 0.15 m.

Variables	**Limits**	**Optimal designs**		
		$\mathrm{R_F}$	$\mathrm{R_M}$	$\mathrm{R_S}$
r [m]	$[0.025, 0.5]$	0.3962	0.3347	0.3706
$\mu\,(h/r)$ $\{h$ [m]$\}$	$]0, 5]$	1.0483 $\{0.4153\}$	1.0501 $\{0.3515\}$	1.1021 $\{0.4084\}$
$\epsilon\,(a/\,(2r))$ $\{a$ [m]$\}$	$]0, 10]$	0.8322 $\{0.6594\}$	0.8739 $\{0.5851\}$	0.5375 $\{0.3984\}$
σ_α $\{\overline{\alpha_{\max}}$ [rad]$\}$	$]0, 1[$	0.7040 $\{1.0726\}$	0.7054 $\{1.0735\}$	0.7666 $\{1.1297\}$
k_1 [N/m]	$[0, 10000]$	1006.6450	1081.0647	1776.7390
σ_{k_1}	$[0, 1]$	0.3156	0.0001	0.3437
k_2 [N/m]	$[0, 10000]$	478.8962	433.1571	424.6377
σ_{k_2}	$[0, 1]$	1.0000	1.0000	1.0000
$F_{\max}$ [N]	$[0, 500]$	38.5137	103.5777	273.5630
$\{\alpha_{\max_1}, \alpha_{\max_2}\}$ [rad]		$\{0.6865, 1.0726\}$	$\{0.2873, 1.0735\}$	$\{0.5190, 1.1297\}$
Spring 1: $\{d$ [mm], D [mm], N_a, l_{0_1} [m], $l_{\max_1}$ [m], m_{k_1} [kg]$\}$		{4.7, 37.35, 94.78, 0.52, 1.05, 1.56}	{2.0, 8.01, 292.95, 0.60, 0.79, 0.18}	{4.8, 29.94, 113.39, 0.60, 0.98, 1.56}
Spring 2: $\{d$ [mm], D [mm], N_a, l_{0_2} [m], $l_{\max_2}$ [m], m_{k_2} [kg]$\}$		{5.3, 85.20, 27.14, 0.31, 1.12, 1.40}	{4.5, 70.09, 28.01, 0.26, 0.95, 0.85}	{4.9, 78.21, 28.91, 0.29, 1.09, 1.16}
Bar cross-section radius r_{b_j} [mm] $j = 1, \ldots, 14$		{7.06, 7.06, 8.29, 6.47, 8.21, 6.47, 5.42, 5.20, 5.20, 5.00, 5.00, 5.00, 5.00, 5.00}	{6.41, 6.41, 7.70, 6.16, 7.71, 6.16, 5.20, 5.00, 5.00, 5.00, 5.00, 5.00, 5.00, 5.00}	{7.40, 7.40, 8.77, 5.31, 8.13, 5.31, 6.41, 5.52, 5.52, 5.00, 5.00, 5.00, 5.00, 5.00}
Mass [kg]		9.1220	4.5659	8.2551
Size [m]		2.9799	2.5761	2.4306

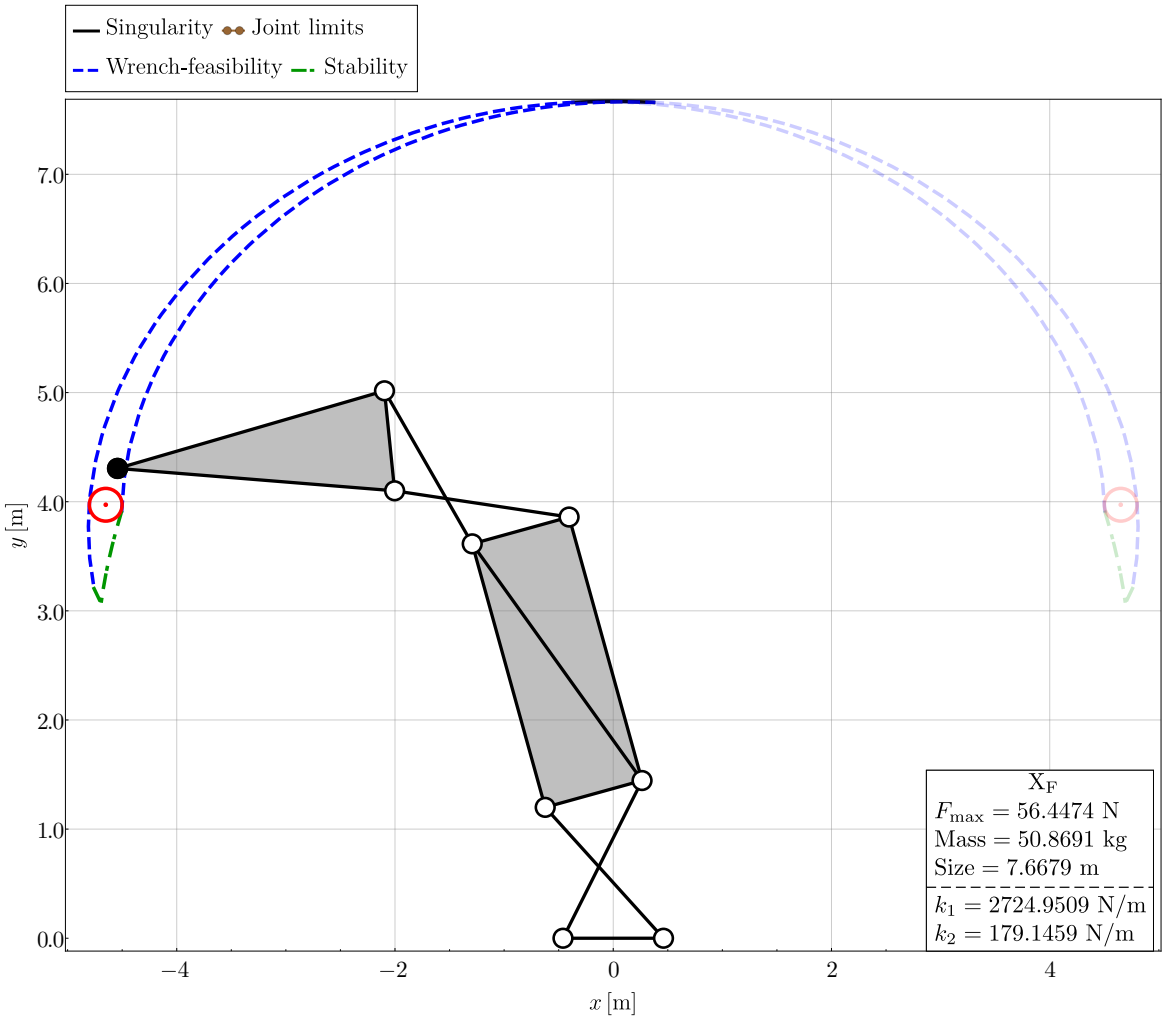

(a) Design X_F

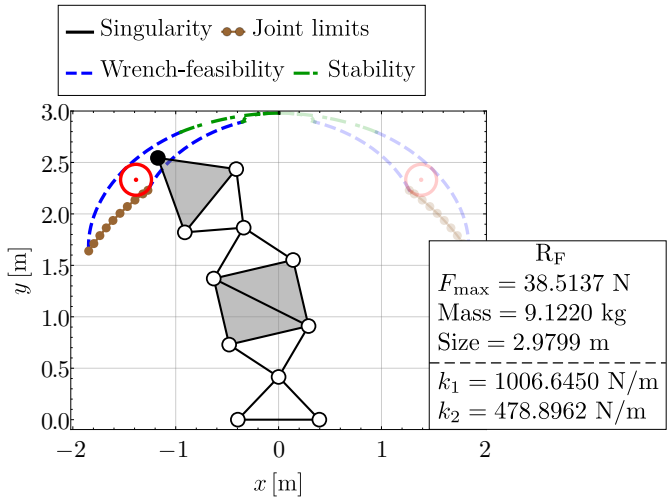

(b) Design R_F

Figure 6: Minimum force designs for the two manipulators.

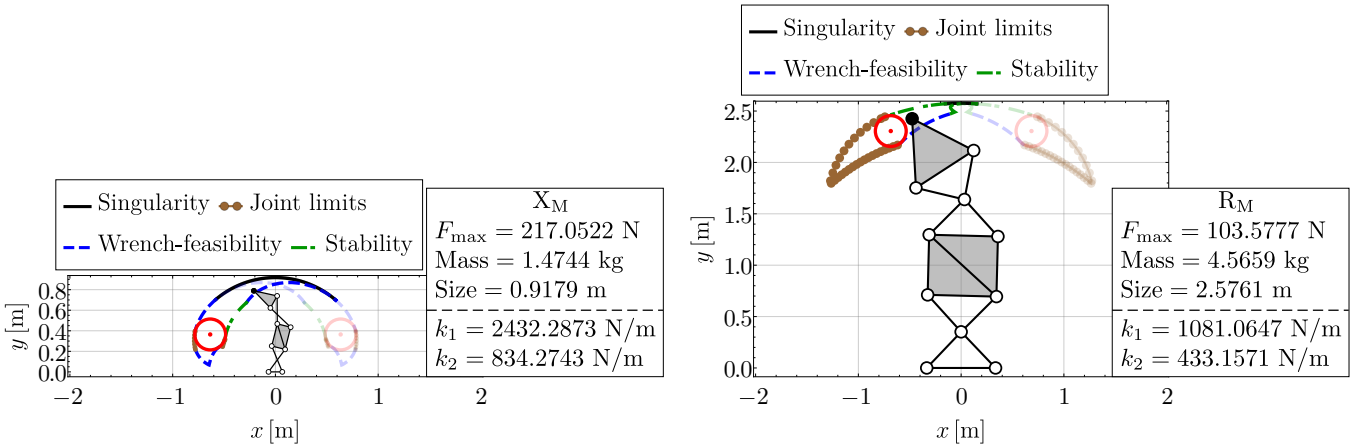

(a) Design X_M (b) Design R_M

Figure 7: Minimum mass designs.

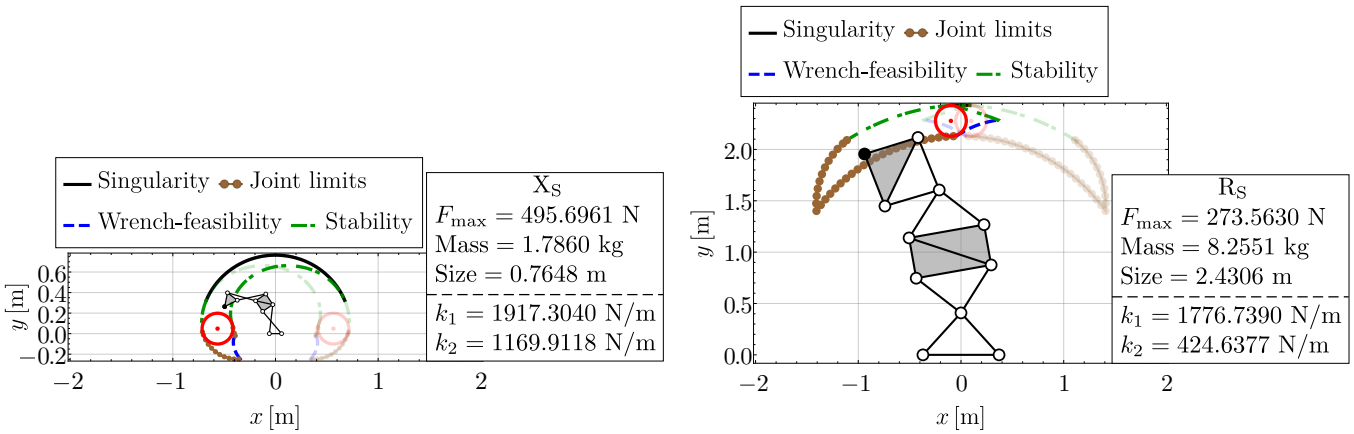

(a) Design X_S (b) Design R_S

Figure 8: Minimum size designs.

and a larger force requirement (≈2 times) when compared to the design R_S. Based on the size value, it is clear that the design X_S should be preferred over R_S as the size optimal design.

It can be derived from the geometry and joint limits of the 2-R manipulator that its size must be at least $\frac{2\sqrt{2}}{\sqrt{2}-1}(\approx 6.8284)$ times the radius of the inscribed disk (see B). Thus, while considering other factors such as wrench-feasibility and stability, the size of the 2-R manipulator relative to the inscribed disk would be even larger. The large size is the primary reason for the large mass of the 2-R manipulators.

In summary, the 2-X manipulator is better in terms of mass and size, while the 2-R manipulator is better in terms of the required actuation force. It would be interesting to study the other optimal designs in the Pareto front for the two manipulators that exhibit good compromise between the three objectives. This study is conducted in the next section.

5.4 Exploration of the Pareto front

The Pareto fronts for the 2-X and 2-R manipulators are enlarged in Figs. 9 and 10, respectively. The Pareto front of the 2-X manipulator has been trimmed by removing X_F and a few points close to it to present a better view of its central portion. Six designs have been chosen on the Pareto fronts of the two manipulators for study, and their complete data are presented in C. The following observations are made on the optimal designs and Pareto fronts of the two manipulators:

- **All designs**: The common properties for all the extremal designs (second item of the list in Section 5.3) are also exhibited by all the optimal designs of the two manipulators presented in Tables 6 and 7.
- **Pareto fronts**: From the Pareto front of the 2-X manipulator in Fig. 9, it is observed that for a given value F_{max}, there is a spread of designs representing the compromise between the mass and size values. This spread is significant for small values of F_{max} but becomes thinner with the increase of F_{max}. On the other hand, in the Pareto front of the 2-R

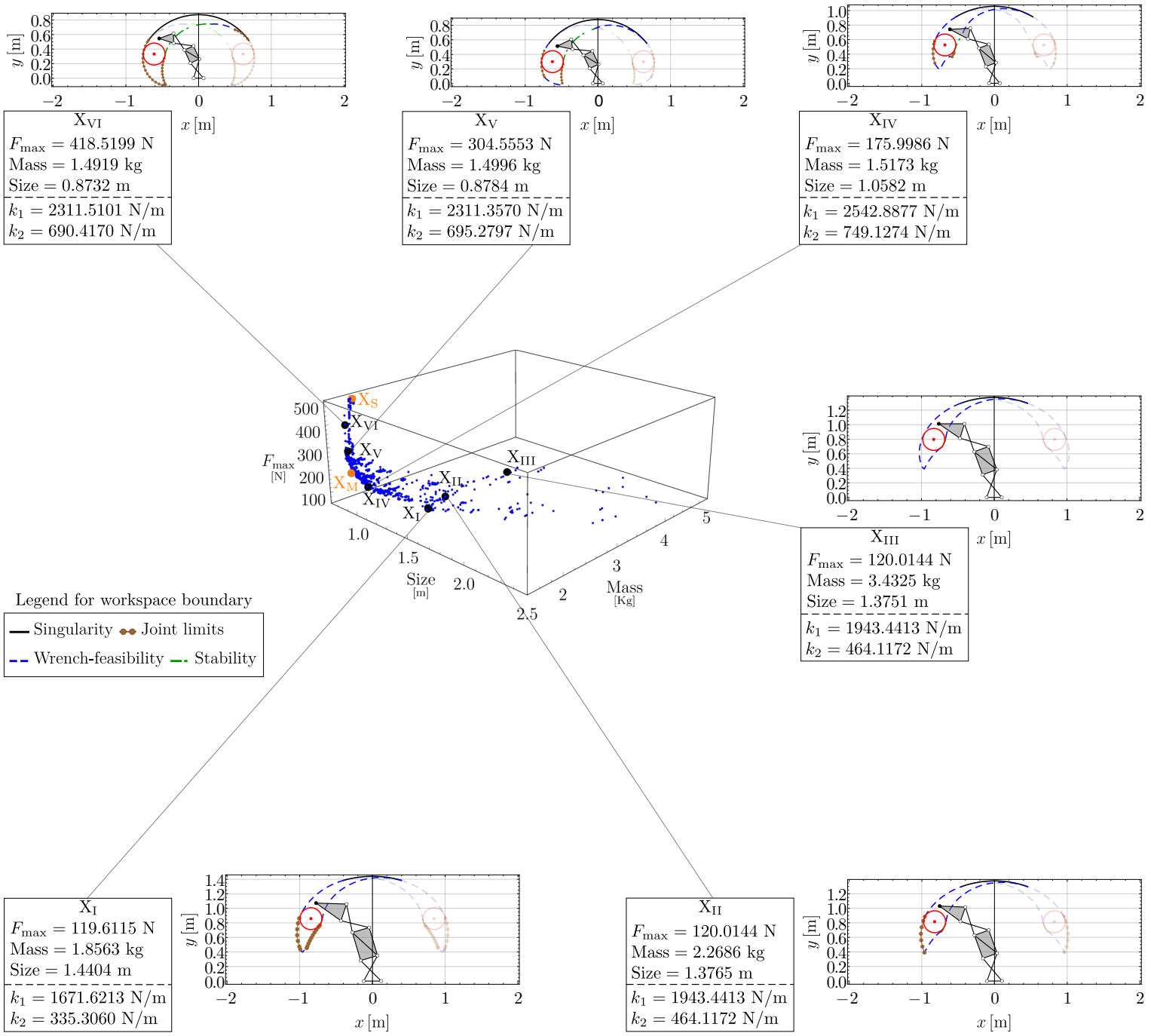

Figure 9: Pareto front and six optimal designs ($X_I, \ldots, X_{VI}$) of the 2-X manipulator obtained for a payload (m_p) of 2 kg and SWFW disk radius (r_d) of 0.15 m. The range of the objectives are $F_{max} \in [56.4474, 498.0113]$ N, mass $\in [1.4744, 50.8691]$ kg, and size $\in [0.7648, 7.6679]$ m. The minimum force design and a few points closer to it have been deleted to present a better view of the major part of the Pareto front.

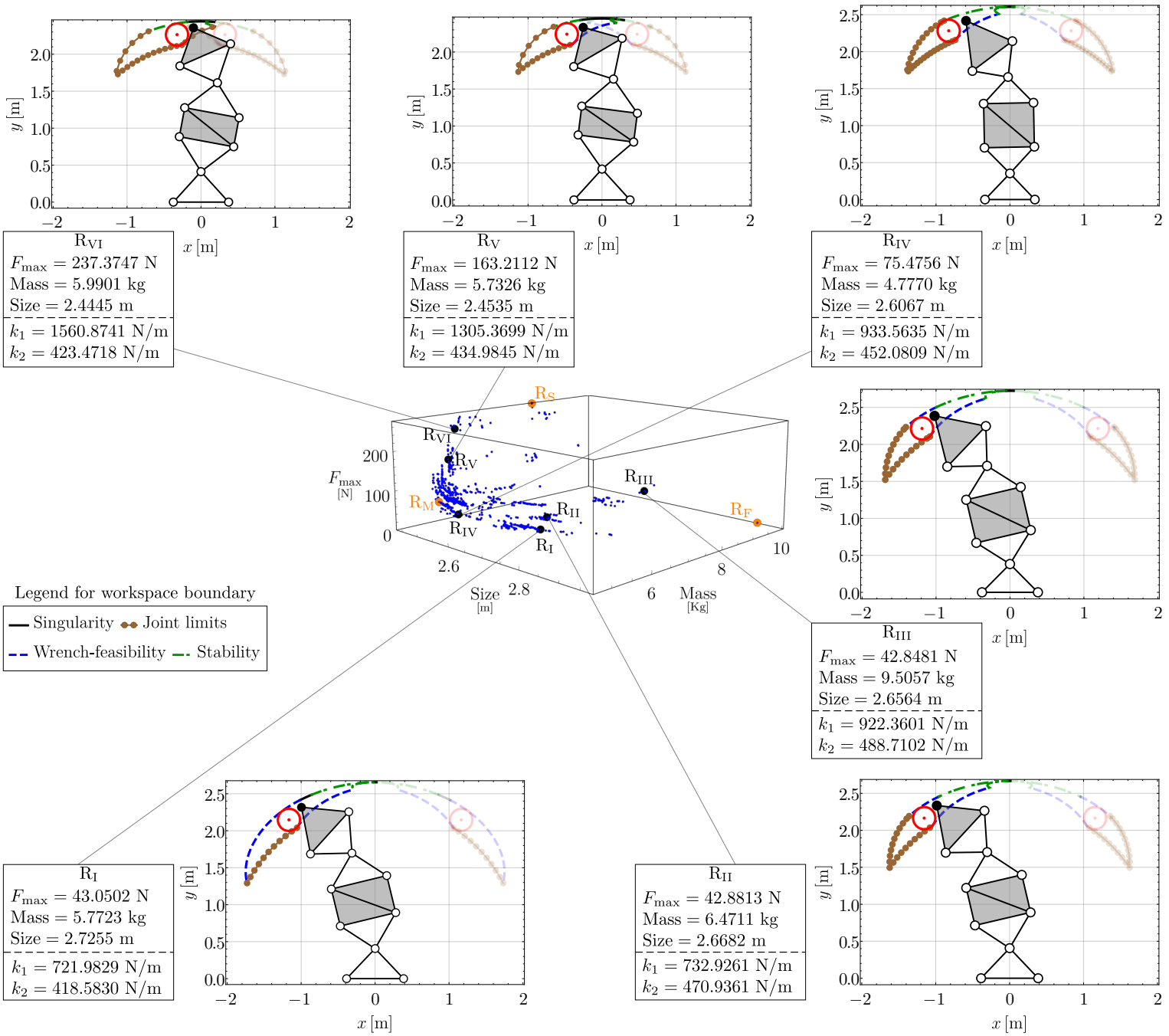

Figure 10: Pareto front and six optimal designs ($\mathrm{R_I}, \ldots, \mathrm{R_{VI}}$) of the 2-R manipulator obtained for a payload (m_p) of 2 kg and SWFW disk radius (r_d) of 0.15 m. The range of objectives are $F_\mathrm{max} \in [38.5137, 275.1206]$ N, mass $\in [4.5659, 10.0591]$ kg, size $\in [2.4306, 2.9799]$ m.

manipulator (see Fig. 10), visually, the spread of designs appears to be more uniform for all values of $F_{\max}$. However, it must be noted that the size of this Pareto front is smaller than its counterpart, as depicted by the range of the objective values. In particular, the variation in the size of the 2-R manipulator is extremely low ($\approx 23\%$) when compared to the other objectives ($\approx 614\%$ for $F_{\max}$ and 120% for mass). Hence, size should not be a major criterion in selecting the best design for the 2-R manipulator.

- **Designs I, II, III**: The designs $(\mathrm{X_I}, \mathrm{X_{II}}, \mathrm{X_{III}})$ and $(\mathrm{R_I}, \mathrm{R_{II}}, \mathrm{R_{III}})$ have been chosen in the Pareto fronts of 2-X and 2-R manipulators, respectively, such that they have almost the same value for $F_{\max}$ (120 N for 2-X and 43 N for 2-R). This choice is made to understand the compromise between mass and size values on the two Pareto fronts. For the 2-X manipulator, the design $\mathrm{X_I}$ corresponds to the minimum mass and maximum size for the assumed $F_{\max}$. As one moves to the designs $\mathrm{X_{II}}$ and $\mathrm{X_{III}}$, the mass increases by $\approx 22\%$ and $\approx 96\%$ respectively, while the size decreases by $\approx 4\%$ and 5% in the respective cases. It is apparent that the decrease in size is not as significant as the increase in mass in those designs. Thus, the design $\mathrm{X_I}$ will be favored over $\mathrm{X_{II}}$ and $\mathrm{X_{III}}$. Another interesting feature is that the designs $\mathrm{X_{II}}$ and $\mathrm{X_{III}}$ are almost identical to one another except for the spring selection parameters σ_{k_i}. This difference causes them to have springs with different parameters, such as wire diameter (d) and coil diameter (D), even while their stiffness remains the same. Interestingly, the springs in design $\mathrm{X_{III}}$ turn out to be heavier than the ones in $\mathrm{X_{II}}$. Specifically, each of the two springs in the first joint of $\mathrm{X_{III}}$ weigh ≈ 0.6 kg more than their counterparts in $\mathrm{X_{II}}$, resulting in ≈ 1.2 kg increase in the overall mass of the manipulator. This shows that the selection of the spring parameters, even while its stiffness is fixed, can significantly affect the design of the tensegrity-inspired manipulators.

  For the 2-R manipulator, the design $\mathrm{R_I}$ corresponds to the minimum mass and maximum size for the assumed $F_{\max}$. In comparison the designs $\mathrm{R_{II}}$ and $\mathrm{R_{III}}$ are $\approx 12\%$ and $\approx 65\%$ heavier respectively, while being $\approx 2\%$ and $\approx 3\%$ smaller in size. The significantly smaller mass makes the design $\mathrm{R_I}$ most favorable among the three.

  Similar results have been found for different values of $F_{\max}$ in the Pareto fronts of both manipulators. Hence, for any given value of force, the minimum mass design would be favored over the others.

- **Minimum mass designs**: Following the previous observation, new minimum mass designs for different values of $F_{\max}$ have been chosen for the two manipulators. These are denoted by $(\mathrm{X_{IV}}, \mathrm{X_V}, \mathrm{X_{VI}})$ and $(\mathrm{R_{IV}}, \mathrm{R_V}, \mathrm{R_{VI}})$ on the Pareto fronts of the 2-X and 2-R manipulators, respectively.

  On the Pareto front of the 2-X manipulator, all the designs on the minimum mass curve, i.e., $(\mathrm{X_I}, \mathrm{X_{IV}}, \mathrm{X_M}, \mathrm{X_V}, \mathrm{X_{VI}})$ are studied sequentially. In the part $(\mathrm{X_I}, \mathrm{X_{IV}}, \mathrm{X_M})$, $F_{\max}$ increases while the mass and size decrease. On the other hand, in the part $(\mathrm{X_M}, \mathrm{X_V}, \mathrm{X_{VI}})$, $F_{\max}$ increases while mass increases and size decreases. In addition to this trend, it is necessary to quantify the increase/decrease to choose the most favorable design. In this regard, as one moves from $\mathrm{X_I}$ to $\mathrm{X_{IV}}$, force increases by $\approx 47\%$ while mass decreases by $\approx 18\%$ and size by $\approx 26\%$, which is a reasonable compromise. From $\mathrm{X_{IV}}$ to $\mathrm{X_M}$, the force increases by $\approx 23\%$ while mass decreases by $\approx 3\%$ and size by $\approx 13\%$, which is a poor compromise. Further moving towards $\mathrm{X_V}$ and $\mathrm{X_{VI}}$, the force increases by more than 35% with a small increase in mass and a reduction in size by less than 5%. This shows that the Pareto front rises steeply along the force axis without producing significant improvement in the mass and size values beyond the design $\mathrm{X_{IV}}$. Hence, among the optimal designs that are presented, $\mathrm{X_{IV}}$ is the most favorable one.

  On the Pareto front of the 2-R manipulator, the designs on the minimum mass curve are $(\mathrm{R_I}, \mathrm{R_{IV}}, \mathrm{R_M}, \mathrm{R_V}, \mathrm{R_{VI}})$. Similar to the Pareto front of the 2-X manipulator, as $F_{\max}$ increases, the mass and size decrease till the design $\mathrm{R_M}$, but beyond that, the mass increases while the size continues to decrease. However, the decrease in size between successive designs is small ($< 5\%$) and is hence not considered further. Between the designs $\mathrm{R_I}$ and $\mathrm{R_{IV}}$, $F_{\max}$ increases by $\approx 75\%$ while the mass decreases by $\approx 17\%$ which is a moderate compromise. Between $\mathrm{R_{IV}}$ and $\mathrm{R_M}$, $F_{\max}$ increases by $\approx 37\%$ while the mass decreases by $\approx 4\%$, which is a poor compromise. Succeeding designs are not studied since both force and mass increase in those cases. The compromise found on this Pareto front is not as good as that of the 2-X manipulator. However, it can be asserted that the favorable designs lie on the minimum mass curve between $\mathrm{R_I}$ and $\mathrm{R_{IV}}$.

In summary, the favorable designs for both manipulators are on the minimum mass curves of the respective Pareto fronts. For the 2-X manipulator, the design $\mathrm{X_{IV}}$ seems to be the best among the ones considered. On the other hand, for the 2-R manipulator the best design is not very obvious; both $\mathrm{R_I}$ and $\mathrm{R_{IV}}$ are better than the others. Between the 2-X and 2-R manipulators, the choice once again depends on which objective is the critical one. If a smaller mass and/or size is more important, then design $\mathrm{X_{IV}}$ is the best choice. But, if smaller $F_{\max}$ is more important, then $\mathrm{R_I}$ may be chosen.

In addition to studying the compromise, the Pareto fronts presented in Figs. 9 and 10 are helpful to the designer for finding favorable optimal designs in the presence of secondary constraints. For instance, if the goal is to build an optimal manipulator with existing actuators, then it amounts to slicing the Pareto front at the corresponding value of $F_{\max}$ to obtain all the relevant optimal designs. Similarly, if there is a constraint on the mass/footprint of the manipulator, as in space exploration missions, the range of mass and size objectives can be suitably adjusted to find the desired designs.

The following section presents the variation of force, mass, and size objectives for different payload and SWFW disk radius specifications.

6 Effect of changing the payload and desired SWFW disk radius specifications

This section aims to verify if the observations reported on the optimal designs of the 2-X and 2-R manipulators are valid even if the payload or disk radius specifications are altered. In this regard, four payloads $m_\mathrm{p} = \{0, 2, 5, 10\}$ kg and four SWFW disk radii $r_\mathrm{d} = \{0.05, 0.15, 0.25, 0.35\}$ m are considered. Design optimization problems have been posed and solved for all 16 combinations of specifications for both manipulators. However, it should be noted that three of the combinations $(m_\mathrm{p} = 5$ kg$, r_\mathrm{d} = 0.35$ m$)$, $(m_\mathrm{p} = 10$ kg$, r_\mathrm{d} = 0.25$ m$)$, $(m_\mathrm{p} = 10$ kg$, r_\mathrm{d} = 0.35$ m$)$ are not feasible for the 2-R manipulator. This can be inferred from Fig. 3 which indicates that the maximum obtainable SWFW disk radius is limited to 0.26 m (resp. 0.17 m) for 5 kg (resp. 10 kg) payload in the case of the 2-R manipulator.

The Pareto fronts have been obtained for all problems in the same manner as illustrated in Section 5.2. However, studying the compromise designs from the Pareto front in each case will be difficult. Hence, only the extremal designs, i.e., the ones optimal w.r.t. force, mass, and size objectives, are considered in the following.

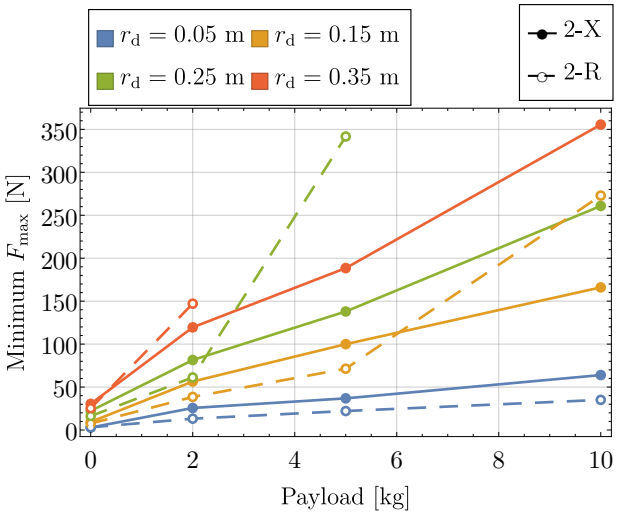

Figure 11: Minimum F_max values for different payload and disk specifications for the 2-X and 2-R manipulators.

The optimal F_max values are plotted as a function of the payload (m_p) for various SWFW disk radius (r_d) specifications in Fig. 11. For the specification $(m_\mathrm{p} = 0$ kg$, r_\mathrm{d} = 0.05$ m$)$, the resulting F_max values are extremely small (< 5 N) for the two manipulators, with the 2-X design having a slightly smaller value than the 2-R design. When $m_\mathrm{p} = 0$, for all other specified r_d, the 2-R manipulator has a smaller F_max than the 2-X manipulator. While for $m_\mathrm{p} = 2$ kg (resp. 5 kg, 10 kg), 2-R manipulator has a smaller F_max when $r_\mathrm{d} \leq 0.25$ m (resp. 0.15 m, 0.05 m), but a greater F_max otherwise.

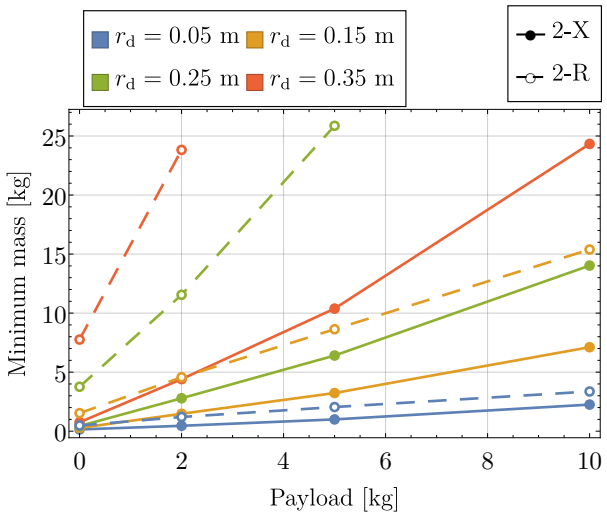

Figure 12: Minimum moving mass values for different payload and disk specifications for the 2-X and 2-R manipulators.

The optimal moving mass values are plotted as a function of the payload (m_p) for various SWFW disk radius (r_d) specifications in Fig. 12. The optimal moving mass of the 2-X manipulator is smaller than that of the 2-R manipulator in all the scenarios. An interesting metric to study the mass optimality of manipulators is the ratio of moving mass to payload (see [29]). It is apparent from the figure that this ratio is roughly the same for a given disk size, but it changes significantly as the disk size changes. While the r_d is specified as (0.05, 0.15, 0.25, 0.35) m, the ratio of moving mass to payload (averaged over feasible payload

specifications) for the 2-X manipulator is computed to be (0.22, 0.70, 1.36, 2.24), respectively, and for the 2-R manipulator it is found to be (0.45, 2.00, 5.47, 11.91), respectively. These data indicate that the 2-X manipulator should be preferred over the 2-R manipulator to have a low moving mass.

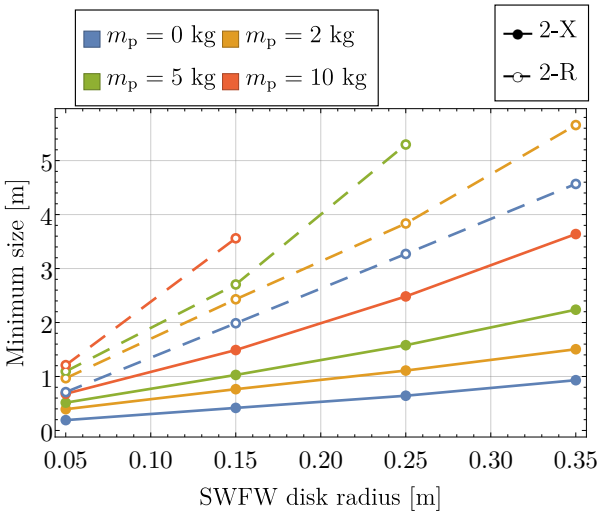

Figure 13: Minimum size values for different payload and disk specifications for the 2-X and 2-R manipulators.

The optimal size values are plotted as a function of the SWFW disk radius (r_d) for various payload (m_p) specifications in Fig. 13, unlike in the previous two figures, as this presentation offers better insights into these data. All the size optimal designs of the 2-X manipulator are found to be smaller than those of the 2-R manipulator for a given SWFW disk radius specification, irrespective of the payload they carry. For instance, while the disk radius is specified to be 0.15 m, the size optimal design of the 2-X manipulator designed to carry a payload of 10 kg is smaller than that of the 2-R manipulator designed for no payload (i.e., 0 kg). A relevant metric to measure compactness is the ratio of manipulator size to SWFW disk radius (see [30] for similar metrics). While the payload specification changes (0, 2, 5, 10) kg, for the 2-X manipulator, this metric (averaged over feasible disk radius specifications) is evaluated to be (2.96, 5.43, 7.47, 10.96), respectively, while for the 2-R manipulator it is (13.40, 16.77, 20.37, 23.97), respectively. This suggests that the 2-X manipulator must be preferred over its counterpart when a compact design is needed.

In summary, the 2-R manipulator has a smaller force requirement when the task is not challenging (i.e., light payload and small SWFW disk radius) but has a more significant force requirement when the task is challenging (i.e., heavy payload and/or large radius). On the other hand, the 2-X manipulator has a smaller moving mass and smaller size, irrespective of whether the task is challenging or not.

7 Possible applications and extensions

The optimal designs of the 2-X and 2-R manipulators obtained in the previous sections are suitable for inspection, welding, and painting applications, where the manipulator carries a constant payload inside its workspace.

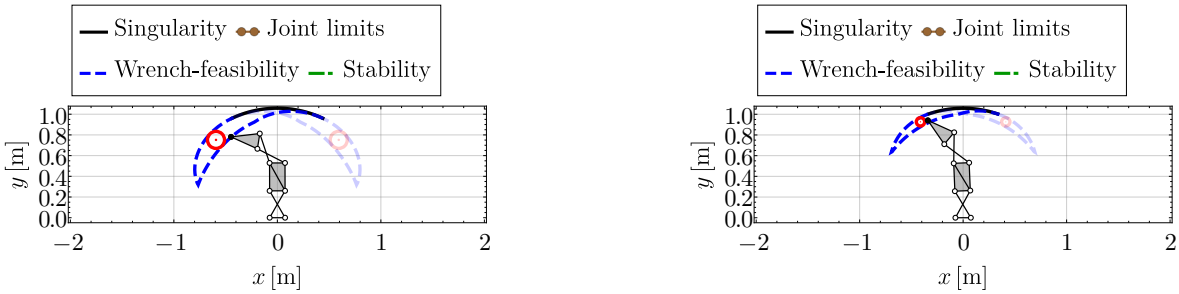

(a) Payload 1.5 kg ($r_d = 0.08$ m)

(b) Payload 0.5 kg ($r_d = 0.04$ m)

Figure 14: Reduction in the SWFW of the design X_{IV} from $r_d = 0.15$ m as the payload decreases from 2 kg.

Since the SWFW is dependent on the static model of the manipulator, it is susceptible to a change in the payload. Consider the design X_{IV} from Fig. 9 with an inscribed SWFW disk of radius $r_d = 0.15$ m while carrying a payload of 2 kg. As the payload is reduced to 1.5 kg (resp. 0.5 kg) the SWFW disk radius decreases to 0.08 m (resp. 0.04 m) as shown in Fig. 14. The reason for this non-intuitive reduction in the SWFW with payload is two-fold. Firstly, the manipulator is placed vertically upward against

gravity. Secondly, stiff springs are used to stabilize the manipulator with the payload loaded at the end-effector. Thus, while the payload is removed, the stiffness of the manipulator increases, and the actuation forces become insufficient to effect the same displacements that were possible with the payload. Thus, the vertically upward placement of the manipulator is unsuitable for an application involving varying payload, e.g., pick-and-place operations.

In order to cope with this problem, the following design scenarios might be considered:

- **Wrench-feasible workspace without stability (against gravity)**: While the manipulator is placed against gravity, the condition of stability might be compromised in the workspace computation, i.e., the wrench-feasible workspace (WFW) can be considered instead of SWFW. In this case, the manipulator can be stabilized using closed-loop control laws similar to the conventional industrial manipulators. The design problem for this scenario can be developed in the same manner as above simply by suppressing the stability conditions in the workspace computation [1].
- **SWFW (along gravity)**: The manipulator might be mounted on the ceiling, vertically downward, similar to the Delta robot [31]. This arrangement makes it inherently stable with a payload and allows for reaching a larger workspace with the same actuation forces while the payload is unloaded. In this case, the design optimization can be performed with the workspace computation tool developed in [1] just by reversing the sign of gravity.

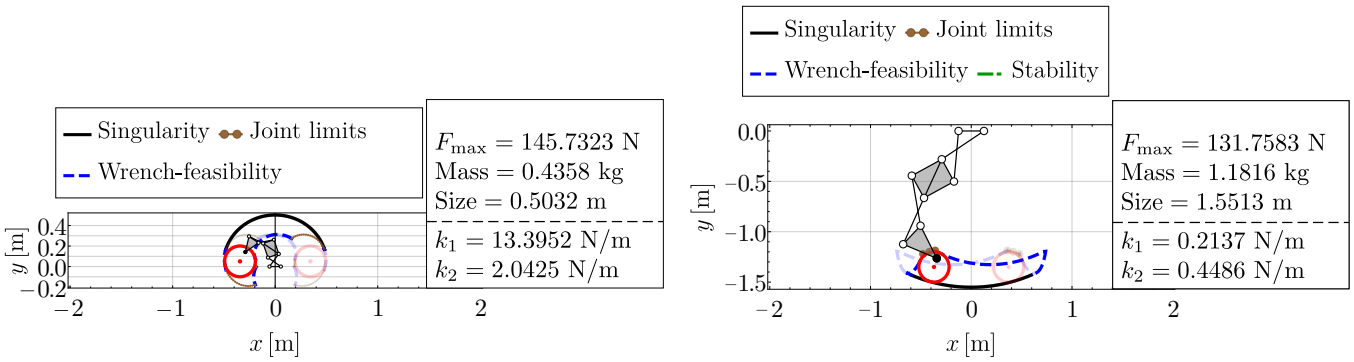

(a) WFW (against gravity)

(b) SWFW (along gravity)

Figure 15: Optimal designs for other design scenarios.

Design optimization problems were posed and solved for the 2-X manipulator for the above two scenarios, following the procedure in Sections 4 and 5. The final optimal designs chosen for the two cases are presented in Fig. 15 and Table 5 (see Appendix F in [3] for more details). For the sake of comparison, the optimal design X_{IV} obtained for SWFW (against gravity) from Table 6 has also been presented in the table. It is observed that in comparison to this design SWFW (against gravity), the optimal design WFW (against gravity) has a lower $F_{\max}$, mass, and size, while the optimal design SWFW (along gravity) has a lower $F_{\max}$ and mass but a larger size. It is also interesting to note that the stiffnesses of the springs are negligible in the optimal designs of the scenarios WFW (against gravity) and SWFW (along gravity), indicating that springs can be eliminated from the manipulator if mechanical stability is not essential or if suspended along gravity. It is also noted that the absence of stability boundary in the workspace plot of the optimal design SWFW (along gravity) shows that its SWFW is the same as its WFW.

Another popular application of robot manipulators is machining. However, designing tensegrity-inspired manipulators for such tasks involves several challenges. Firstly, the direction and magnitude of forces required for machining should be taken into account. Then, the designer should find a good placement of the part inside the workspace. If there is more than one feasible configuration for the manipulator at the chosen location, a suitable one must be chosen. Based on these data, the cross-sections of bars must be designed to avoid buckling failure. In this regard, analysis of force capabilities of tensegrity-inspired manipulators through polytopes [32] is a relevant work. The notions of available wrench set and prescribed wrench set (see, e.g., [33],[34]) used in the context of cable-driven parallel manipulators can be applied to these manipulators as well.

8 Conclusions

Two planar cable-driven tensegrity-inspired manipulators composed of two anti-parallelogram (X) joints and two revolute (R) joints, respectively, were studied in this work. The manipulators are placed vertically against gravity and are stabilized by adding springs in their joints. Four antagonistically arranged cables actuate each of these manipulators. Various design optimization problems were posed and solved to find optimal designs of the two manipulators, and a comparison between them was performed.

The article [1] presented a method to compute the stable wrench-feasible workspace (SWFW) and the maximal disk inside it, for the two manipulators. This paper has used that method to find optimal designs of the two manipulators minimizing the maximal

Table 5: Chosen optimal designs of the 2-X manipulator for carrying a payload of mass 2 kg and inscribing a disk of radius 0.15 m in different scenarios.

Variables	**Limits**	**Optimal designs**		
		SWFW (against gravity)	WFW (against gravity)	SWFW (along gravity)
b [m]	$[0.05, 1.0]$	0.1492	0.1117	0.2519
$\lambda\,(l/b)$ $\{l$ [m]$\}$	$]1, 10]$	2.0077 $\{0.2996\}$	1.3733 $\{0.1534\}$	2.0005 $\{0.5040\}$
$\epsilon\,(a/b)$ $\{a$ [m]$\}$	$]0, 10]$	1.8052 $\{0.2693\}$	1.3114 $\{0.1465\}$	1.3459 $\{0.3391\}$
σ_α $\{\overline{\alpha_{\max}}$ [rad]$\}$	$]0, 1[$	0.6773 $\{2.1279\}$	0.9407 $\{2.9552\}$	0.6831 $\{2.1461\}$
k_1 [N/m]	$[0, 10000]$	2542.8877	13.9352	0.2137
σ_{k_1}	$[0, 1]$	0.0988	0.4278	0.5379
k_2 [N/m]	$[0, 10000]$	749.1274	2.0425	0.4486
σ_{k_2}	$[0, 1]$	0.9432	1.0000	0.9909
$F_{\max}$ [N]	$[0, 500]$	175.9986	145.7323	131.7583
$\{\alpha_{\max_1}, \alpha_{\max_2}\}$ [rad]		$\{0.8818, 2.1279\}$	$\{1.7273, 2.9552\}$	$\{1.2148, 2.1461\}$
Spring 1: $\{d$ [mm], D [mm], N_a, l_{0_1} [m], $l_{\max_1}$ [m], m_{k_1} [kg]$\}$		{3.0, 17.85, 57.02, 0.20, 0.33, 0.19}	{0.5, 8.99, 65.50, 0.05, 0.22, $3e-3$}	{0.2, 3.67, 1543.35, 0.32, 0.60, $4e-3$}
Spring 2: $\{d$ [mm], D [mm], N_a, l_{0_2} [m], $l_{\max_2}$ [m], m_{k_2} [kg]$\}$		{3.0, 32.60, 31.80, 0.16, 0.42, 0.20}	{0.2, 3.58, 173.65, 0.04, 0.26, $5e-4$}	{0.2, 3.99, 574.04, 0.12, 0.71, $2e-3$}
Bar cross-section radius r_{b_j} [mm] $j = 1, \ldots, 12$		{6.44, 6.44, 5.00, 5.06, 5.53, 5.06, 5.00, 5.00, 5.00, 5.00, 5.00, 5.00}	{6.83, 6.83, 5.38, 5.00, 5.00, 5.00, 5.00, 5.00, 5.00, 5.00, 5.00, 5.00}	{6.87, 6.87, 5.00, 5.00, 5.00, 5.13, 5.00, 5.00, 5.00, 5.00, 5.00, 5.00}
Mass [kg]		1.5173	0.4358	1.1816
Size [m]		1.0582	0.5032	1.5513

actuation force ($F_{\max}$), moving mass, and size (measured by maximal vertical reach) while they respected the specifications on payload and SWFW disk radius. The optimal designs for the two manipulators were presented as Pareto fronts. The Pareto front of the 2-X manipulator has a larger range for all objectives, indicating a wider variety of optimal designs than its counterpart.

In most optimal designs of the two manipulators, the range of movement for the first joint (fixed to the base), which supports a more significant mass, is lesser than that of the second joint, which supports a smaller mass. The springs in the first joint are stiffer and have a longer free length, while the ones in the second joint are wider and have a longer operating length.

Among the optimal designs in the Pareto front, the extremal designs, i.e., the force, mass, and size optimal designs of the two manipulators were compared. It was found that the 2-R manipulator has a slightly smaller ($\approx$ 1/1.5 times) actuation force requirement, while the 2-X manipulator has a much smaller ($\approx$ 1/3 times) moving mass and size.

Then, several compromise designs from the Pareto fronts were presented. The compromise between mass and size was not very convincing for a given $F_{\max}$. The mass increased by $(12-96)\%$ to cause a reduction of $(2-5)\%$ in size for both manipulators. Thus, the minimum mass designs were favorable for all values of $F_{\max}$. Based on the compromise between $F_{\max}$ and minimum mass and the associated change in size, one best design was proposed for the 2-X manipulator, while two good designs were proposed for the 2-R manipulator.

In order to verify if the above conclusions are valid for other specifications, four payloads $\in [0, 10]$ kg and four SWFW disk radii $\in [0.05, 0.35]$ m were chosen. The design optimization was conducted for the two manipulators for all sixteen combinations of payload and SWFW disk radius specifications. It was found that the 2-R manipulator has a smaller $F_{\max}$ when the specified disk radius is sufficiently smaller for a given payload, while the 2-X manipulator has a smaller $F_{\max}$ in other cases. On the other hand, the 2-X manipulator has a smaller moving mass and much smaller size in all cases. The ratio of moving mass to payload of the mass optimal 2-X (resp. 2-R) designs vary in the range $(0.22-2.24)$ (resp. $(0.45-11.91)$) while the specified disk radii $\in [0.05, 0.35]$ m. Note that the ratio is less than one for smaller disks, which indicates that the resulting designs have a moving mass that is less than the payload they carry. This feature makes tensegrity-inspired manipulators interesting candidates for applications such as inspection, painting, etc. In addition, the ratio of manipulator size to SWFW disk radius for the size optimal 2-X (resp. 2-R) designs vary in the range $(2.96-10.96)$ (resp. $(13.40-23.97)$), while the payload mass $\in [0, 10]$ kg. These results show that the size optimal 2-X manipulators are much more compact than their counterparts.

The proposed design method is generic and applies to all the tasks involving the manipulation of a payload. If the loading changes during the operation, as in a pick-and-place task, the SWFW can change significantly while the manipulator is placed against gravity. Hence, for such applications, it would be more suitable to consider only the wrench-feasibility condition for its workspace and stabilize it using a closed-loop control scheme. Another possibility is to mount the manipulator on the ceiling

and suspend it vertically downward to ensure intrinsic stability with gravity. Design optimization was performed in both cases using the proposed method for the 2-X manipulator, and the results were compared with the optimal design chosen for SWFW (against gravity). It was observed that in the new scenarios, the springs are no longer needed for stability, and consequently, the optimal designs turned out to be better in terms of force and mass.

In the future, this design method will be extended to consider the local performances of the manipulators, such as their velocities, force application capabilities, variable stiffness, and dynamic indices. Further, spatial manipulators composed of tensegrity-inspired joints will be studied, and experiments will be conducted on test beds.

A Illustration of the design space of springs

This section briefly presents the conditions that define the feasible design space of a spring. More details on this subject can be found in [1],[35].

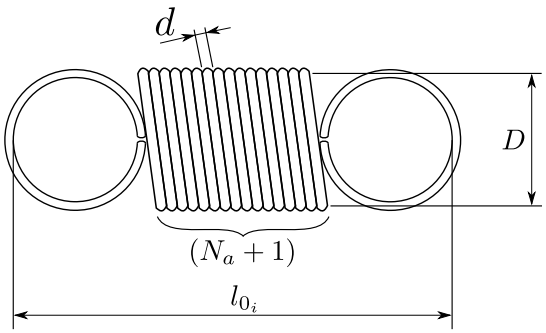

Figure 16: Schematic of a helical extension spring.

The schematic of a helical extension spring with stiffness k_i and free length l_{0_i} is shown in Fig. 16. It has a wire diameter d, nominal coil diameter D, and a number of active coils N_a. Conventionally, the number of active coils is assumed to be one less than the total number of coils in the body (see, e.g., [36], p. 357).

While the material is known, the spring parameters $\{k_i, d, D, N_a, l_{0_i}\}$ can completely define a spring. However, they must also respect two equations. The first one is the relation between the spring stiffness and its geometry and material properties (see [36], p. 355), while the second one is the geometric relation between the free length and other parameters (see Fig. 16):

$$k_i = \frac{G_k d^4}{8 N_a D^3} \implies N_a = \frac{G_k d^4}{8 k_i D^3} \tag{6}$$

$$l_{0_i} = (N_a + 1)d + 2(D - d) \tag{7}$$

Thus, only three of the above parameters can be chosen independently to define a spring. In this work, (k, d, D) are treated as independent parameters while (N_a, l_{0_i}) are determined from Eqs. (6) and (7), respectively.

In addition, several inequality conditions must be respected by the spring (see [35] for more details):

$$\begin{cases} \chi_1 : \text{coils must be strong enough to support the specified deflection} \\ \chi_2 : \text{there should be more than three active coils} \\ \chi_3 : \text{the spring index } (D/d) \text{ must be bounded inside } [4, 20] \\ \chi_4 : \text{the helix angle must be less than } 7.5^\circ \end{cases} \tag{8}$$

Note that the inequalities χ_1 and χ_4 impose a realistic constraint on the maximum elongation $(l_{\max_i})$ of the spring to ensure its safe functioning and respect its mathematical model [35]. All of these conditions can be formulated solely in terms of the independent spring parameters (k, d, D) using Eqs. (6),(7).

The above conditions must necessarily be met by any spring for its mechanical feasibility. In addition, while the spring is installed in the joints of the tensegrity-inspired manipulators, it must satisfy additional constraints [1]. These lead to two sets of feasibility conditions $\boldsymbol{\chi}_a$ and $\boldsymbol{\chi}_b$, either of which can be satisfied by a feasible spring. If the spring belongs to $\boldsymbol{\chi}_a$, it imposes strong limits on joint movements, but if it belongs to $\boldsymbol{\chi}_b$, it allows the joint to reach its safe joint limits $(\pm\overline{\alpha_{\max}})$.

It is customary to use only standard values for the wire diameter (d) for accurate fabrication, as it is the most influential parameter in the spring design (see Eqs. (6),(7)). Thus, in this study, the wire diameter is assumed to be a discrete variable that takes the following values $d = \{0.2, 0.3, \ldots, 6\}$ mm. This setting reduces the three-dimensional design space (k, d, D) of the springs to a family of two-dimensional surfaces which can be defined with just two independent parameters.

As a numerical illustration, consider the example of the 2-X manipulator corresponding to design X_{IV} from Table 6. A slice of the spring design space with $k_i = k_2 = 749.1274$ N/m is shown in Fig. 17(a). The vertical grid lines represent the chosen

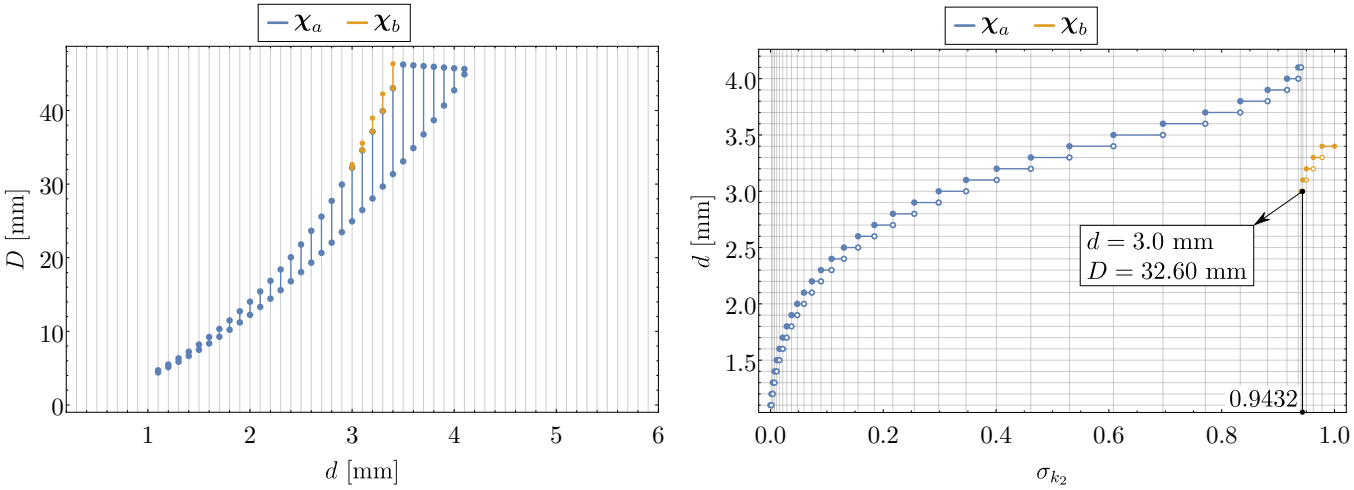

(a) Feasible intervals in (d, D) space

(b) Normalized intervals and their successive arrangement

Figure 17: Parametrization of the feasible design space for springs with $\sigma_{k_2} \in [0, 1]$ when $k_2 = 749.1274$ N/m for an X-joint with $b = 0.1492$ m, $l = 0.2996$ m, and $\overline{\alpha_{\max}} = 2.1279$ rad.

discrete values of d. For each value of d, the feasible intervals of D are shown in colors. The intervals corresponding to the set $\boldsymbol{\chi}_a$ are shown in blue shade while those corresponding to the set $\boldsymbol{\chi}_b$ are shown in orange shade. The complete feasible design space is obtained from the union of the two sets $\boldsymbol{\chi}_a \cup \boldsymbol{\chi}_b$.

All the feasible intervals can be placed successively and normalized w.r.t. to their total length to create a bijective mapping with a fraction $\sigma_{k_2} \in [0, 1]$, as depicted in Fig. 17(b). Hence, all the feasible spring designs corresponding to $k_2 = 749.1274$ N/m can be accessed by simply varying the parameter σ_{k_2} from zero to unity. For instance, when we set $\sigma_{k_2} = 0.9432$ consistent with the design $\mathrm{X_{IV}}$, the corresponding point in the feasible space is found to be $(d, D) = (3.0, 32.60)$ mm. All the other dependent parameters can be obtained from Eqs. (6),(7), thereby completely defining the spring.

In summary, the complete feasible design space for the springs of a tensegrity-inspired joint with known geometry and safe joint limits can be described with just two parameters (k_i, σ_{k_i}), with $\sigma_{k_i} \in [0, 1]$.

B Size of the 2-R manipulator relative to the maximal inscribed disk

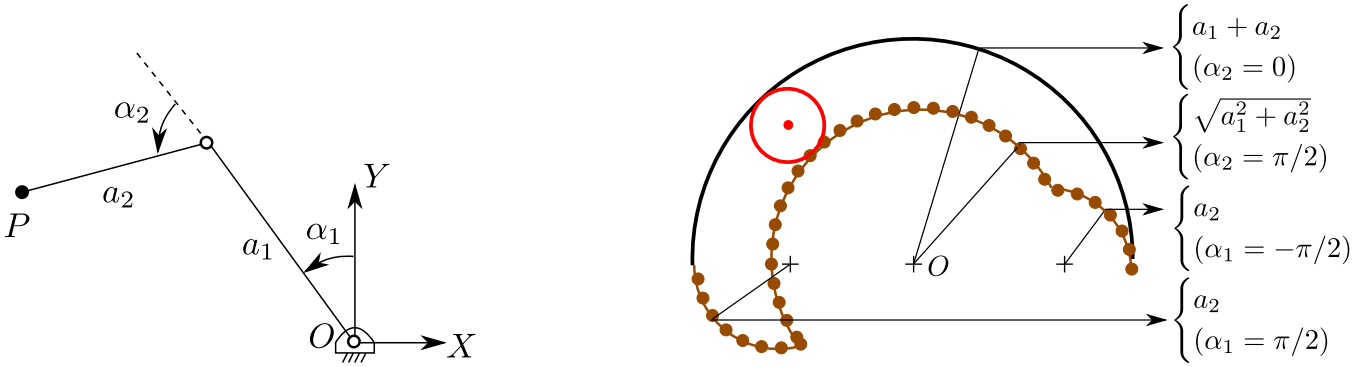

(a) Simplified 2-R manipulator

(b) Workspace boundaries when $(\alpha_2 > 0)$ and respective conditions on joint angles

Figure 18: Simplified sketch of the 2-R manipulator and one half of its workspace in the presence of joint limits $\alpha_1, \alpha_2 \in \left]-\frac{\pi}{2}, \frac{\pi}{2}\right[$.

A simplified sketch of the 2-R manipulator composed of two bars with lengths a_1 and a_2 is presented in Fig. 18(a). The maximal reach or size of the manipulator is fixed at $S := a_1 + a_2$. Let the R-joints reach their maximum possible range of movement $\alpha_1, \alpha_2 \in \left]-\frac{\pi}{2}, \frac{\pi}{2}\right[$ (see [1]). The workspace of this manipulator would be bounded by several circular arcs whose centers and radii are shown in Fig. 18(b) (only one half is shown since the other half is symmetric about the y-axis).

Clearly, the maximal inscribed disk must be tangential to the two arcs formed by $(\alpha_2 = 0)$ and $(\alpha_2 = \frac{\pi}{2})$. This disk has several possible placements, one of which is shown in Fig. 18(b). It has a radius of $r_{\mathrm{d}} = \left((a_1 + a_2) - \sqrt{a_1^2 + a_2^2}\right) \big/ 2$, which can be

rewritten in terms of the size (S) as: $r_{\mathrm{d}} = (S - \sqrt{S^2 - 2a_1a_2})\big/2$.

For a fixed size S, the inscribed disk radius can be maximized by maximizing the product (a_1a_2) subject to the condition: $a_1 + a_2 = S$. This leads to the optimal solution $a_1 = a_2 = S/2$. Substituting this result into the above expression of r_{d} results in: $r_{\mathrm{d}} = \frac{\sqrt{2}-1}{2\sqrt{2}} S \, (\approx \frac{S}{6.8284})$.

Thus, the maximal reach (or size) of the 2-R manipulator must be at least $\frac{2\sqrt{2}}{\sqrt{2}-1} (\approx 6.8284)$ times the radius of the inscribed disk.

C Designs on the Pareto fronts of the 2-X and 2-R manipulators

All the parameters of the optimal designs chosen on the Pareto front of the 2-X manipulator are presented in Table 6, and those of the 2-R manipulator are presented in Table 7.

D Effect of pulley radius on the SWFW of the 2-X manipulator

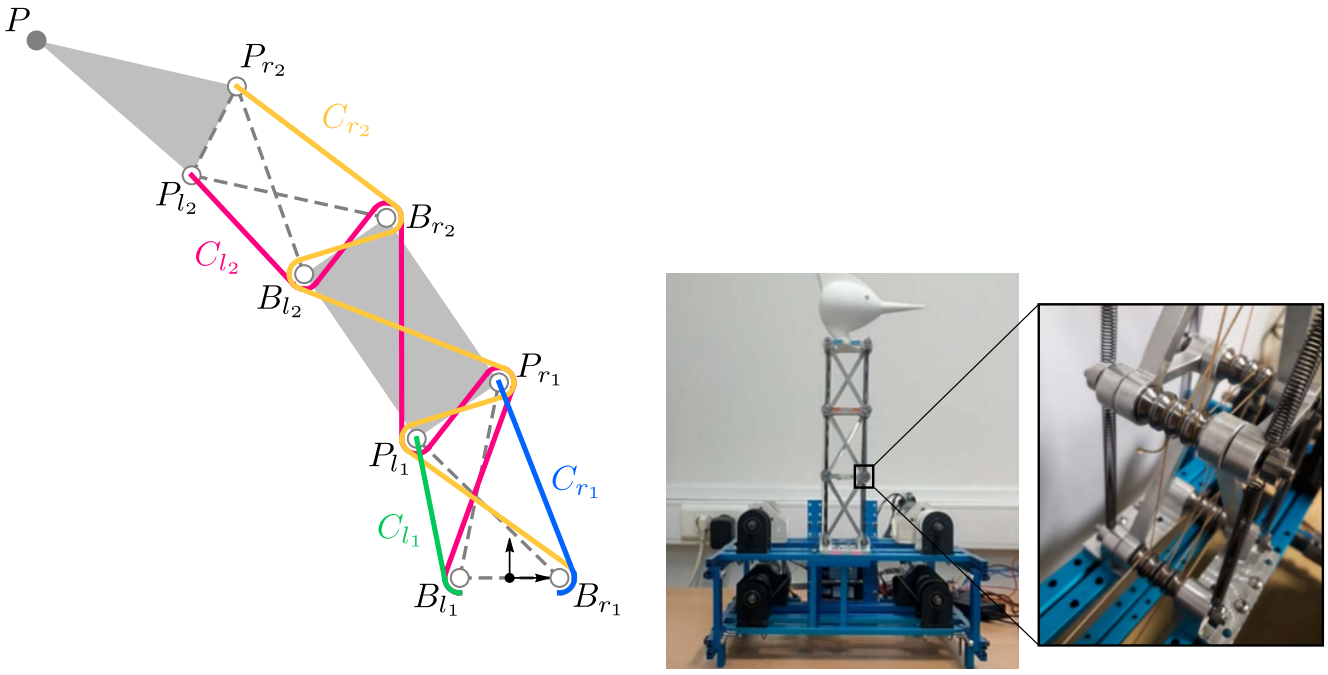

(a) Routing of cables C_{l_2}, C_{r_2} around pulleys

(b) Practical realization as depicted in [37]

Figure 19: Illustration of strut-routed cables around pulleys in the 2-X manipulator.

This section studies the influence of considering a non-zero pulley radius on the static model of the 2-X manipulator. The strut-routing of the cables C_{l_2} and C_{r_2} along the rigid bodies with realistic pulleys is shown in Fig. 19. In the static model of the manipulator presented in Section 2.2, the inclusion of pulley radius only modifies the lengths of the actuating cables $C_{l_1}, C_{r_1}, C_{l_2}, C_{r_2}$. Their new expressions are reported as follows:

$$\begin{cases} \text{length}(C_{l_1}) = \widehat{B_{l_1}} + \overline{B_{l_1}P_{l_1}} \\ \text{length}(C_{r_1}) = \widehat{B_{r_1}} + \overline{B_{r_1}P_{r_1}} \\ \text{length}(C_{l_2}) = \widehat{B_{l_1}} + \overline{B_{l_1}P_{r_1}} + \widehat{P_{r_1}} + \overline{P_{r_1}P_{l_1}} + \widehat{P_{l_1}} + \overline{P_{l_1}B_{r_2}} + \widehat{B_{r_2}} + \overline{B_{r_2}B_{l_2}} + \widehat{B_{l_2}} + \overline{B_{l_2}P_{l_2}} \\ \text{length}(C_{r_2}) = \widehat{B_{r_1}} + \overline{B_{r_1}P_{l_1}} + \widehat{P_{l_1}} + \overline{P_{l_1}P_{r_1}} + \widehat{P_{r_1}} + \overline{P_{r_1}B_{l_2}} + \widehat{B_{l_2}} + \overline{B_{l_2}B_{r_2}} + \widehat{B_{r_2}} + \overline{B_{r_2}P_{r_2}} \end{cases} \tag{9}$$

where $\widehat{J}$ represents the arc length of the cable wound around the pulley at J, $\overline{JI}$ represents the length of the common tangent between pulleys at J and I, and $\overline{JI}$ represents the length of the tangent from vertex I to the pulley at J. The expressions for these terms have been presented in the technical report [38]. It is worth noting that the tangent lengths between pulleys fixed at a constant distance, such as $\overline{B_{l_1}P_{r_1}}$, will remain invariant to the change in configuration of the manipulator. Also, the arc lengths of cables around certain pulleys, e.g., $\widehat{P_{l_1}}, \widehat{B_{r_2}}$ for cable C_{l_2}, remain constant as their relative orientation w.r.t. the neighboring pulleys does not change. Hence, the derivative of these terms will vanish in the equation of static equilibrium and

the expression of the stiffness matrix, causing no impact on the SWFW of the manipulator. On the other hand, there are a few terms such as $\widehat{B_{l_1}}$ for cable C_{l_2} which cause dependence of its length on the first joint and influence the static model.

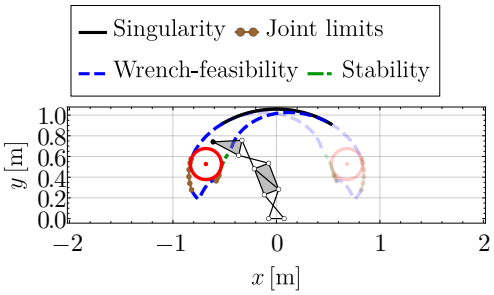

(a) SWFW of design X_{IV} with zero pulley radius containing maximal inscribed disks of radius 0.1502 m each

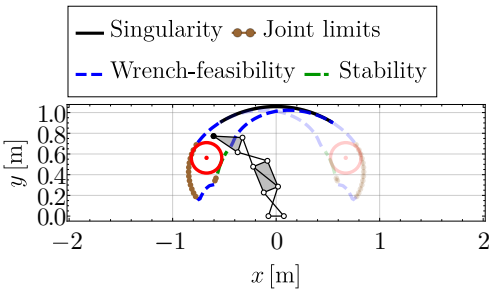

(b) SWFW of design X_{IV} with pulley radius 46 mm containing maximal inscribed disks of radius 0.1472 m each

Figure 20: Effect of pulley radius on the SWFW of a 2-X manipulator.

As an illustration, let us consider the design X_{IV} from Table 6. The plot of its SWFW with zero pulley radius is presented in Fig. 20(a). Let us consider all the pulleys to have a radius of 46 mm consistent with the prototype presented in [37]. The revised SWFW of this manipulator has been presented in Fig. 20(b). From these plots, we observe that there is a negligible difference in the SWFW contours as well as the size of the maximal inscribed disks. This example shows that neglecting the pulley radius in the manipulator for performing its design optimization is acceptable.

References

[1] V. Muralidharan, P. Wenger, C. Chevallereau, Design considerations and workspace computation of 2-X and 2-R planar cable-driven tensegrity-inspired manipulators, Mechanism and Machine Theory 195 (2024) 105610. doi:10.1016/j.mechmachtheory.2024.105610.

[2] C. Sultan, Tensegrity: 60 years of art, science, and engineering, in: Advances in Applied Mechanics, Vol. 43 of Advances in Applied Mechanics, Elsevier, 2009, pp. 69–145. doi:10.1016/S0065-2156(09)43002-3.

[3] V. Muralidharan, Design and analysis of tensegrity-inspired manipulators, Ph.D. thesis, Ecole Centrale de Nantes (2023).

[4] P. Obara, J. Kłosowska, W. Gilewski, Truth and myths about 2D tensegrity trusses, Applied Sciences 9 (1). doi:10.3390/app9010179.

[5] Q. Li, C. Yang, L. Xu, W. Ye, Performance Analysis and Optimization of Parallel Manipulators, Springer Nature, Singapore, 2023. doi:10.1007/978-981-99-0542-3.

[6] C. M. Gosselin, M. Guillot, The synthesis of manipulators with prescribed workspace, Journal of Mechanical Design 113 (4) (1991) 451–455. doi:10.1115/1.2912804.

[7] V. Muralidharan, A. Bose, K. Chatra, S. Bandyopadhyay, Methods for dimensional design of parallel manipulators for optimal dynamic performance over a given safe working zone, Mechanism and Machine Theory 147 (2020) 103721. doi:10.1016/j.mechmachtheory.2019.103721.

[8] B. Fasquelle, M. Furet, P. Khanna, D. Chablat, C. Chevallereau, P. Wenger, A bio-inspired 3-DOF light-weight manipulator with tensegrity X-joints, in: Proceedings of 2020 IEEE International Conference on Robotics and Automation (ICRA 2020), Paris, France, 2020.

[9] N. Song, M. Zhang, F. Li, Z. Kan, J. Zhao, H. Peng, Dynamic research on winding and capturing of tensegrity flexible manipulator, Mechanism and Machine Theory 193 (2024) 105554. doi:https://doi.org/10.1016/j.mechmachtheory.2023.105554.

[10] Q. Yang, K. Hu, Y. Zhang, B. Lian, T. Sun, Design and experiment of multi-locomotion tensegrity mobile robot, Mechanism and Machine Theory 198 (2024) 105671. doi:https://doi.org/10.1016/j.mechmachtheory.2024.105671.

[11] J. Jeong, I. Kim, Y. Choi, S. Lim, S. Kim, H. Kang, D. Shah, R. Baines, J. W. Booth, R. Kramer-Bottiglio, S. Y. Kim, Spikebot: A multigait tensegrity robot with linearly extending struts, Soft Robotics 11 (2) (2024) 207–217. doi:10.1089/soro.2023.0030.

[12] Y. Liu, Q. Bi, X. Yue, J. Wu, B. Yang, Y. Li, A review on tensegrity structures-based robots, Mechanism and Machine Theory 168 (2022) 104571. doi:10.1016/j.mechmachtheory.2021.104571.

[13] J. Krivošej, P. Beneš, J. Zavřel, A. Balon, V. Halamka, Z. Šika, Energy efficient robots based on structures with tensegrity features and cable-driven mechanisms, Mechanism and Machine Theory 187 (2023) 105364. doi:https://doi.org/10.1016/j.mechmachtheory.2023.105364.

[14] S. Venkateswaran, D. Chablat, P. Hamon, An optimal design of a flexible piping inspection robot, Journal of Mechanisms and Robotics 13 (3) (2021) 035002. doi:10.1115/1.4049948.

[15] J. Begey, M. Vedrines, P. Renaud, Design of tensegrity-based manipulators: Comparison of two approaches to respect a remote center of motion constraint, IEEE Robotics and Automation Letters 5 (2) (2020) 1788–1795. doi:10.1109/LRA.2020.2969190.

[16] K. D. Snelson, Continuous tension, discontinuous compression structures, United States patent No. US3169611A (1965).

[17] Y. Dong, J. Ding, C. Wang, X. Liu, Kinematics analysis and optimization of a 3-DOF planar tensegrity manipulator under workspace constraint, Machines 9 (11). doi:10.3390/machines9110256.

[18] V. Muralidharan, P. Wenger, Optimal design and comparative study of two antagonistically actuated tensegrity joints, Mechanism and Machine Theory 159 (2021) 104249. doi:10.1016/j.mechmachtheory.2021.104249.

[19] V. Muralidharan, P. Wenger, C. Chevallereau, Computation of stable wrench-feasible workspace of cable driven n-X manipulator, in: Proceedings of the 25ème Congrès Français de Mécanique, Nantes, France, 2022.

[20] V. Muralidharan, Stable wrench-feasible workspace of a 2-X tensegrity manipulator, Technical report, LS2N, École Centrale de Nantes (2022).

[21] J. Baek, C.-C. Iurascu, F. C. Park, Finding the maximally inscribed rectangle in a robot's workspace, KSME International Journal 15 (8) (2001) 1119–1131. doi:10.1007/BF03185092.

[22] M. K. Karnam, A. Baskar, R. A. Srivatsan, S. Bandyopadhyay, Computation of the safe working zones of planar and spatial parallel manipulators, Robotica 38 (5) (2020) 861–885. doi:10.1017/S0263574719001139.

[23] K. Deb, A. Pratap, S. Agrawal, T. Meyarivan, A fast and elitist multiobjective genetic algorithm: NSGA-II, IEEE Transactions on Evolutionary Computation 6 (2) (2002) 182–197. doi:10.1109/4235.996017.

[24] S. Agarwal, S. Bandyopadhyay, Design of six-bar function generators using dual-order structural error and analytical mobility criteria, Mechanism and Machine Theory 116 (2017) 326–351. doi:10.1016/j.mechmachtheory.2017.04.016.

[25] S. Briot, S. Caro, C. Germain, Design procedure for a fast and accurate parallel manipulator, Journal of Mechanisms and Robotics 9 (6) (2017) 061012. doi:10.1115/1.4038009.

[26] R. Saravanan, S. Ramabalan, N. G. R. Ebenezer, C. Dharmaraja, Evolutionary multi criteria design optimization of robot grippers, Applied Soft Computing 9 (1) (2009) 159–172. doi:10.1016/j.asoc.2008.04.001.

[27] E. Zitzler, M. Laumanns, L. Thiele, SPEA2: Improving the strength pareto evolutionary algorithm, TIK report 103 (2001) . doi:10.3929/ethz-a-004284029.

[28] H. Jain, K. Deb, An evolutionary many-objective optimization algorithm using reference-point based nondominated sorting approach, part II: Handling constraints and extending to an adaptive approach, IEEE Transactions on Evolutionary Computation 18 (4) (2014) 602–622. doi:10.1109/TEVC.2013.2281534.

[29] S. Shepherd, A. Buchstab, KUKA Robots On-Site, Springer International Publishing, Cham, 2014, pp. 373–380. doi:10.1007/978-3-319-04663-1_26.

[30] M. Russo, Measuring performance: Metrics for manipulator design, control, and optimization, Robotics 12 (1). doi:10.3390/robotics12010004.

[31] X.-J. Liu, J. Wang, K.-K. Oh, J. Kim, A new approach to the design of a delta robot with a desired workspace, Journal of Intelligent and Robotic Systems 39 (2) (2004) 209–225. doi:10.1023/B:JINT.0000015403.67717.68.

[32] V. Muralidharan, P. Wenger, C. Chevallereau, Kinematic and static analysis of a cable-driven 2-X tensegrity manipulator for two actuation strategies, in: O. Altuzarra, A. Kecskeméthy (Eds.), Advances in Robot Kinematics 2022, Springer International Publishing, Cham, 2022, pp. 149–159.

[33] A. Riechel, I. Ebert-Uphoff, Force-feasible workspace analysis for underconstrained, point-mass cable robots, in: Proceedings of IEEE International Conference on Robotics and Automation (ICRA 04), Vol. 5, 2004, pp. 4956–4962. doi:10.1109/ROBOT.2004.1302503.

[34] G. Boucher, T. Laliberté, C. Gosselin, Mechanical design of a low-impedance 6-degree-of-freedom displacement sensor for intuitive physical human–robot interaction, Journal of Mechanisms and Robotics 13 (2). doi:10.1115/1.4049191.

[35] V. Muralidharan, Computation of the feasible design space for helical extension springs and its parametric representation, Technical Report, LS2N, École Centrale de Nantes (2022).

[36] P. R. N. Childs, Mechanical Design: Theory and Applications, 3rd Edition, Butterworth-Heinemann, 2021. doi:10.1016/B978-0-12-821102-1.00015-9.

[37] B. Fasquelle, P. Khanna, C. Chevallereau, D. Chablat, D. Creusot, S. Jolivet, P. Lemoine, P. Wenger, Identification and control of a 3-X cable-driven manipulator inspired from the bird's neck, Journal of Mechanisms and Robotics 14 (1) (2021) 011005. doi:10.1115/1.4051521.

[38] B. Fasquelle, Cable lengths calculation, modelling and identification of parameters on a manipulator inspired by bird necks, Technical Report, LS2N, École Centrale de Nantes (2021).

Table 6: Optimal designs on the Pareto front of the 2-X manipulator for carrying a payload of mass 2 kg and inscribing an SWFW disk of radius 0.15 m.

Variables	**Limits**	**Optimal designs**					
		X_I	X_{II}	X_{III}	X_{IV}	X_V	X_{VI}
b [m]	$[0.05, 1.0]$	0.2415	0.2082	0.2082	0.1492	0.1362	0.1362
$\lambda\,(l/b)$ $\{l$ [m]$\}$	$]1, 10]$	1.6535 {0.3992}	1.9562 {0.4074}	1.9571 {0.4075}	2.0077 {0.2996}	2.0213 {0.2753}	2.0214 {0.2753}
$\epsilon\,(a/b)$ $\{a$ [m]$\}$	$]0, 10]$	1.6660 {0.4022}	1.6238 {0.3381}	1.6196 {0.3373}	1.8052 {0.2693}	1.4687 {0.2000}	1.4490 {0.1973}
σ_α $\{\overline{\alpha_{\max}}$ [rad]$\}$	$]0, 1[$	0.6038 {1.8968}	0.7228 {2.2707}	0.7233 {2.2724}	0.6773 {2.1279}	0.7280 {2.2870}	0.7278 {2.2863}
k_1 [N/m]	$[0, 10000]$	1671.6213	1943.4413	1943.4413	2542.8877	2311.3570	2311.5101
σ_{k_1}	$[0, 1]$	0.0175	0.0429	0.3610	0.0988	0.4074	0.3583
k_2 [N/m]	$[0, 10000]$	335.3060	464.1172	464.1172	749.1274	695.2797	690.4170
σ_{k_2}	$[0, 1]$	0.9530	0.8545	0.8708	0.9432	0.9697	0.9663
$F_{\max}$ [N]	$[0, 500]$	119.6115	120.0144	120.0144	175.9986	304.5553	418.5199
$\{\alpha_{\max_1}, \alpha_{\max_2}\}$ [rad]		$\{0.5976, 1.8968\}$	$\{0.6881, 2.2707\}$	$\{0.7406, 2.2724\}$	$\{0.8818, 2.1279\}$	$\{1.2575, 2.2870\}$	$\{1.2310, 2.2863\}$
Spring 1: $\{d$ [mm], D [mm], N_a, l_{0_1} [m], $l_{\max_1}$ [m], m_{k_1} [kg]$\}$		{2.5, 13.73, 91.90, 0.25, 0.40, 0.16}	{3.0, 17.08, 85.23, 0.29, 0.43, 0.26}	{4.8, 40.07, 43.26, 0.28, 0.43, 0.83}	{3.0, 17.85, 57.02, 0.20, 0.33, 0.19}	{3.7, 29.72, 31.47, 0.17, 0.33, 0.27}	{3.6, 28.05, 33.53, 0.17, 0.33, 0.26}
Spring 2: $\{d$ [mm], D [mm], N_a, l_{0_2} [m], $l_{\max_2}$ [m], m_{k_2} [kg]$\}$		{2.5, 29.24, 47.49, 0.17, 0.57, 0.18}	{3.3, 42.54, 33.82, 0.19, 0.59, 0.33}	{3.4, 45.60, 30.93, 0.19, 0.59, 0.35}	{3.0, 32.60, 31.80, 0.16, 0.42, 0.20}	{2.8, 30.78, 30.89, 0.15, 0.39, 0.16}	{2.8, 30.88, 30.80, 0.15, 0.39, 0.16}
Bar cross-section radius r_{b_j} [mm] $j = 1, \ldots, 12$		{6.81, 6.81, 5.00, 5.61, 6.20, 5.61, 5.00, 5.00, 5.00, 5.00, 5.00, 5.00}	{7.01, 7.01, 5.00, 5.39, 6.00, 5.39, 5.00, 5.00, 5.00, 5.00, 5.00, 5.00}	{7.06, 7.06, 5.00, 5.38, 5.99, 5.38, 5.00, 5.00, 5.00, 5.00, 5.00, 5.00}	{6.44, 6.44, 5.00, 5.06, 5.53, 5.06, 5.00, 5.00, 5.00, 5.00, 5.00, 5.00}	{6.69, 6.69, 5.00, 5.00, 5.08, 5.00, 5.00, 5.00, 5.00, 5.00, 5.00, 5.00}	{6.98, 6.98, 5.00, 5.00, 5.30, 5.00, 5.00, 5.00, 5.00, 5.00, 5.00, 5.00}
Mass [kg]		1.8563	2.2686	3.4325	1.5173	1.4996	1.4919
Size [m]		1.4404	1.3765	1.3751	1.0582	0.8785	0.8732

Table 7: Optimal designs on the Pareto front of the 2-R manipulator for carrying a payload of mass 2 kg and inscribing an SWFW disk of radius 0.15 m.

Variables	**Limits**	**Optimal designs**					
		R_I	R_{II}	R_{III}	R_{IV}	R_V	R_{VI}
r [m]	$[0.025, 0.5]$	0.3781	0.3862	0.3857	0.3373	0.3787	0.3739
$\mu\,(h/r)$ $\{h$ [m]$\}$	$]0, 5]$	1.0112 {0.3824}	1.0527 {0.4066}	1.0546 {0.4067}	1.0486 {0.3537}	1.1015 {0.4171}	1.1013 {0.4117}
$\epsilon\,(a/\,(2r))$ $\{a$ [m]$\}$	$]0, 10]$	0.7908 {0.5980}	0.6745 {0.5210}	0.6674 {0.5148}	0.8832 {0.5959}	0.5183 {0.3925}	0.5333 {0.3988}
σ_α $\{\overline{\alpha_{\max}}$ [rad]$\}$	$]0, 1[$	0.6745 {1.0520}	0.7075 {1.0750}	0.7072 {1.0733}	0.6995 {1.0657}	0.7659 {1.1292}	0.7666 {1.1304}
k_1 [N/m]	$[0, 10000]$	721.9829	732.9261	922.3601	933.5635	1305.3699	1560.8741
σ_{k_1}	$[0, 1]$	0.0321	0.0378	0.5411	0.0055	0.0001	0.0072
k_2 [N/m]	$[0, 10000]$	418.5830	470.9361	488.7102	452.0809	434.9845	423.4718
σ_{k_2}	$[0, 1]$	1.0000	1.0000	1.0000	1.0000	1.0000	1.0000
$F_{\max}$ [N]	$[0, 500]$	43.0502	42.8813	42.8481	75.4756	163.2112	237.3947
$\{\alpha_{\max_1}, \alpha_{\max_2}\}$ [rad]		$\{0.5450, 1.0520\}$	$\{0.5492, 1.0750\}$	$\{0.7332, 1.0733\}$	$\{0.3571, 1.0657\}$	$\{0.2871, 1.1292\}$	$\{0.2931, 1.1304\}$
Spring 1: $\{d$ [mm], D [mm], N_a, l_{0_1} [m], $l_{\max_1}$ [m], m_{k_1} [kg]$\}$		{2.9, 17.96, 172.40, 0.53, 0.94, 0.51}	{3.0, 18.43, 179.79, 0.57, 0.99, 0.59}	{5.3, 49.11, 73.59, 0.48, 1.04, 2.05}	{2.2, 10.02, 253.88, 0.58, 0.82, 0.24}	{2.4, 9.61, 291.86, 0.72, 0.93, 0.32}	{2.8, 11.79, 244.52, 0.71, 0.92, 0.44}
Spring 2: $\{d$ [mm], D [mm], N_a, l_{0_2} [m], $l_{\max_2}$ [m], m_{k_2} [kg]$\}$		{4.7, 73.97, 29.35, 0.28, 1.04, 1.02}	{5.2, 83.74, 26.94, 0.30, 1.09, 1.31}	{5.3, 85.65, 26.18, 0.30, 1.09, 1.36}	{4.6, 71.17, 27.99, 0.27, 0.95, 0.90}	{5.0, 79.58, 29.04, 0.30, 1.11, 1.23}	{4.9, 77.85, 29.39, 0.29, 1.10, 1.17}
Bar cross-section radius r_{b_j} [mm] $j = 1, \ldots, 14$		{6.48, 6.48, 7.84, 5.92, 7.65, 5.92, 5.16, 5.00, 5.00, 5.00, 5.00, 5.00, 5.00, 5.00}	{6.61, 6.61, 7.98, 5.54, 7.60, 5.54, 5.33, 5.10, 5.10, 5.00, 5.00, 5.00, 5.00, 5.00}	{6.77, 6.77, 8.02, 5.53, 7.62, 5.53, 5.36, 5.13, 5.13, 5.00, 5.00, 5.00, 5.00, 5.00}	{6.34, 6.34, 7.61, 6.14, 7.64, 6.14, 5.07, 5.00, 5.00, 5.00, 5.00, 5.00, 5.00, 5.00}	{6.87, 6.87, 8.35, 5.00, 7.71, 5.00, 5.98, 5.35, 5.35, 5.00, 5.00, 5.00, 5.00, 5.00}	{7.14, 7.14, 8.64, 5.21, 8.01, 5.21, 6.28, 5.47, 5.47, 5.00, 5.00, 5.00, 5.00, 5.00}
Mass [kg]		5.7723	6.4711	9.5057	4.7770	5.7326	5.9901
Size [m]		2.7255	2.6682	2.6564	2.6067	2.4535	2.4445